

**DESIGN IMPROVEMENT OF MINIATURE BORING TOOLS
USING PROCESS MODELS**

by

MAHZAD SARGHASSABI

Submitted to the Graduate School of Engineering and Natural Sciences
in partial fulfillment of
the requirements for the degree of Master of Science

Sabancı University

July 2023

Mahzad Sarghassabi 2023 ©
All Rights Reserved

ABSTRACT

DESIGN IMPROVEMENT OF MINIATURE BORING TOOLS USING PROCESS MODELS

MAHZAD SARGHASSABI

MANUFACTURING ENGINEERING MASTER'S THESIS, JULY 2023

Thesis Supervisor: Prof. ERHAN BUDAK

Keywords: Miniature Boring Tools, Design Improvement, Force Model, Chatter Stability Model, Experimental Analysis

Machining of precise small holes, an essential feature in parts used in a variety of industries like aerospace and medical, is made possible by miniature boring tools. Due to the tight dimensional tolerances and demand for high-quality surface finishes, the hole enlarging process necessitates the use of miniature boring tools and precise cutting conditions. However, the delicate geometrical properties of small boring tools make them vulnerable to static and dynamic deflections. Additionally, the hole enlarging process, which is increasing the diameter of previously drilled holes, necessitates close attention to maintaining the desired level of surface finish, along with achieving improved hole dimensions and tolerances such as excellent circularity and cylindricity values.

Since cutting forces, particularly the radial force, induce the deflection of tools in the process of cutting, the principal aim of this study is to reduce the forces and enhance the stability of the tool. The geometric features of the tool, depth of cut, and feed rate values are critical factors that impact the chip geometry and, consequently, the cutting forces.

A force model and a chatter stability model were developed according to the geometric properties of the cutting tool. The developed models are validated by experiments. The experiments involved the measurement of cutting forces, tool wear, surface roughness, cylindricity, and circularity of the workpiece. Furthermore, modal tests were conducted, and stability limits, and the tools' clamping stiffness were measured through experiments. The

results of the study indicated that the predicted and experimental values exhibited a high degree of agreement. Therefore, through implementation of the established force model, the impact of the geometric characteristics of the cutting edge on the cutting forces, and ultimately, on the quality of the surface finish was examined. This investigation was carried out with the objective of improving the design of the miniature boring tool's edge geometry to achieve accurate holes in the hole enlarging operations.

ÖZET

MİNYATÜR DELİK GENİŞLETME TAKIM TASARIMLARININ SÜREÇ MODELLERİ KULLANARAK İYİLEŞTİRMESİ

MAHZAD SARGHASSABI

ÜRETİM MÜHENDİSLİĞİ YÜKSEK LİSANS TEZİ, TEMMUZ 2023

Tez Danışmanı: Prof. Dr. ERHAN BUDAK

Anahtar Kelimeler: Minyatür delik genişletme takımları, Tasarım İyileştirme, Kuvvet Modeli, Tırlama Stabilite Modeli, Deneysel Analiz

Havacılık ve tıp gibi çeşitli endüstrilerde kullanılan parçalarda önemli bir özellik olan hassas küçük deliklerin işlenmesi, minyatür delik genişletme takımları ile mümkün olmaktadır. Dar boyutsal toleranslar ve yüksek kaliteli yüzey pürüzlülüğü talebi nedeniyle delik genişletme işlemi, minyatür delik genişletme takımlarının ve hassas kesme koşullarının kullanılmasını gerektirir. Bununla birlikte, minyatür delik genişletme takımlarının hassas geometrik özellikleri, onları statik ve dinamik sapmalara karşı savunmasız hale getirir. Ek olarak, daha önce delinmiş deliklerin çapını artıran delik büyütme işlemi, mükemmel dairesellik ve silindiriklik değerleri gibi iyileştirilmiş delik boyutları ve toleransların elde edilmesinin yanı sıra, istenen yüzey kalitesi seviyesinin korunmasına da dikkat edilmesini gerektirir.

Kesme kuvvetleri, özellikle radyal kuvvet, kesme işleminde takımların sapmasına neden olduğundan, bu çalışmanın temel amacı kuvvetleri azaltmak ve takımın stabilitesini arttırmaktır. Takımın geometrik özellikleri, kesme derinliği ve ilerleme hızı değerleri, talaş geometrisini ve dolayısıyla kesme kuvvetlerini etkileyen kritik faktörlerdir. Kesici takımın geometrik özelliklerine göre bir kuvvet modeli ve bir tırlama stabilite modeli geliştirilmiştir. Geliştirilen modeller deneylerle doğrulanmıştır. Deneyler, iş parçasının kesme kuvvetlerinin, takım aşınmasının, yüzey pürüzlülüğünün, silindirikliğinin ve daireselliğinin ölçülmesini içerir.

Ayrıca modal testler yapılmış, deneylerle stabilite limitleri ve takımların bağlanma rijitlikleri ölçülmüştür. Çalışmanın sonuçları, öngörülen ve deneysel değerlerin yüksek derecede bir uyum sergilediğini göstermiştir. Bu nedenle, geliştirilen kuvvet modelinin uygulanması yoluyla kesici takımın geometrik özelliklerinin kesme kuvvetleri üzerindeki etkisi ve nihayetinde yüzey pürüzlülüğün kalitesi incelenmiştir. Bu araştırma, delik genişletme operasyonlarında yüksek kaliteli delikler elde etmek için minyatür delik genişletme takımının geometrisinin tasarımını iyileştirmek amacıyla gerçekleştirildi.

ACKNOWLEDGMENT

I am profoundly grateful to my thesis supervisor, Prof. Erhan Budak, for his invaluable advice, insightful feedback, and unwavering support throughout my thesis journey. His expertise, patience, and dedication played a crucial role in my ability to successfully complete my thesis. I would also like to extend my gratitude to my thesis jury members, Associate Prof. Lütfi Taner Tunç and Associate Prof. Umut Karagüzel for their valuable feedback and constructive comments that greatly enriched the quality of my work.

I wish to convey my deep gratitude to the members of MRL and Maxima, with special acknowledgment to Süleyman Tutkun, Ertuğrul Sadıkoğlu, Ahmet Göksinir, and Murat Saçkan. Their technical support and consistent availability during the experiments for this research have been invaluable. Furthermore, being a part of the MRL research group has proven to be an incredibly fortunate opportunity, allowing me to interact with remarkable individuals like Esra, Saif, Faraz, Zahra, Arash, Saltuk, Farzad, Suzan, and Vahid. Additionally, I would like to extend my appreciation to my friends who have been by my side throughout these years.

Lastly, I want to extend my heartfelt gratitude to my family, especially my mother, whose support has been the bedrock of my entire journey. Their constant encouragement, understanding, and belief in me have been an unending source of strength. Through every challenge and triumph, their presence has provided the comfort and motivation needed to navigate this intricate path. Their sacrifices, patience, and unwavering faith have played an immeasurable role in my accomplishments, making this journey not just mine, but ours to celebrate together.

To My Father

Table of Contents

ABSTRACT.....	iv
ÖZET	vi
Table of Contents	x
List of Figures.....	xii
List of Tables.....	xii
1. Literature Survey	1
1.1 Introduction	1
1.2 Mechanics of Boring Process	2
1.3 Dynamics of Boring Process	2
1.4 Surface Roughness and Geometric Errors in Boring Process	5
1.5 Objective	7
1.6 Thesis Layout	8
2. Mechanics of Boring Process	9
2.1 Kinematics of Boring Process	9
2.2 Modeling of Chip Geometry	11
2.3 Depth of Cut higher than Nose Radius.....	14
2.3.1 Elemental chip thickness for section 1.....	14
2.3.2 Elemental chip thickness for section 2 and 3	15
2.3.3 Elemental chip thickness for section 4.....	16
2.3.4 Elemental Angles of each Section.....	16
2.4 Depth of Cut smaller than Nose Radius	17
2.4.1 Elemental chip thickness for section 1.....	17
2.4.2 Elemental chip thickness for section 2.....	18
2.4.3 Elemental Angles of each Section.....	18
2.5 Cutting Forces	19
2.6 Solution Procedure	20
2.7 Experimental Verifications:.....	20
3. Dynamics of Boring Process	24
3.1 Analytical Modeling of Chatter Stability in Boring Process	24
3.1.1 Dynamic Chip Thickness and Cutting Forces	24

3.1.1	Effect of Nose Radius and Positive Approach angle	26
3.2	Stability Limit Solution.....	27
3.3	Solution Procedure	28
3.4	Experimental Analysis of Miniature Boring Tools Dynamics	29
3.4.1	Stiffness Measurement of Miniature Boring Tools for Different Tool-Holder Configurations	30
3.4.1	Modal Analysis of Miniature Boring Tools for Different Holder-Tool Configurations	32
3.5	Model Verification.....	34
3.5.1	Model Verification from Literature.....	34
3.5.2	Model Verification with Experiments	35
4.	Design Improvement of Miniature Boring Tools	37
4.1	Simulation Results.....	37
4.1.1	Effect of Nose Radius and Approach Angle on the Forces.....	37
4.1.2	Effect of Oblique and Rake Angle on the Forces.....	41
4.1.3	Effect of Feed Rate	45
4.1.4	Discussion on Simulation Results.....	46
4.2	Experimental Results.....	47
4.2.1	Surface Roughness, Cylindricity, and Circularity.....	51
4.2.2	Effect of Tool Wear	52
4.2.3	Summary of Experimental Results	54
5.	Contribution of the Study	55
6.	Future Work	56
7.	Conclusion	57
A.	Appendix	59
	Reference	64

List of Figures

Figure 1.1. a) top and b) side view of a miniature boring tool.	1
Figure 1.2. Geometric properties of a miniature boring tool.	1
Figure 2.1. Geometric properties of a miniature boring tool.	10
Figure 2.2. Schematic of boring process by Atabey [1].....	10
Figure 2.3. Tangential, radial, and feed forces (F_t, F_r, F_f) acting on the tool tip.....	11
Figure 2.4. The uncut chip area in boring process using a miniature boring tool.....	11
Figure 2.5. Illustration of eight different uncut chip area configurations defined with approach angle (C_s), depth of cut (b), feed rate (f), and nose radius of the tool (r)......	12
Figure 2.6. Scallop marks left on the workpiece in successive passes due to feed rate a) bigger than nose radius b) smaller than nose radius.	13
Figure 2.7. Normal and friction forces acting on the uncut chip area when a) $C_s > 0, f < r, b > r$ b) $C_s > 0, f < r, b < r$	13
Figure 2.8. division of the uncut chip area into elements when a) $C_s > 0, f < r, b > r$ b) $C_s > 0, f < r, b < r$	14
Figure 2.9. 3D representation of the local cutting angles on the insert [50].....	16
Figure 2.10. a) The fixture used for clamping tool holder on the dynamometer. b) Measuring forces using dynamometer	21
Figure 2.11. The simulations and experimental results for 1050 Steel workpiece material in a) tangential (x), b) radial (y), and c) feed (z) directions	22
Figure 2.12. The simulations and experimental results for Ti-6Al-4V workpiece material in a) tangential (x), b) radial (y), and c) feed (z) directions	23
Figure 3.1. Direction variation of dynamic chip thickness of section 1, 2, and 3.	25
Figure 3.2. Division of chip thickness by trapezoidal elements	26

Figure 3.3. four tool-holder configurations a) tool1-holder1 b) tool2-holder1 c) tool1-holder2 d) tool2-holder2	30
Figure 3.4. Force-displacement curve used to compute stiffness of tool using tool holder1 (tool holder with loose tolerance).....	31
Figure 3.5. Force-displacement curve used to compute stiffness of tool using tool holder2 (tool holder with tight tolerance).....	31
Figure 3.6. a) top and b) side view of a miniature boring tool.	32
Figure 3.7. Modal test setup and measured FRFs.....	33
Figure 3.8. Mode shapes for a) Tool1-holder1 b) Tool2-holder1 c) Tool1-holder2 d) Tool2- holder2 configurations	34
Figure 3.9. Comparison of the predicted stable depth of cut by Budak’s and adapted model.	35
Figure 3.10. Chatter test and simulation results for stable depth of cut using tool1 and tool2 clamping with a) Holder1 b) Holder2.....	36
Figure 4.1. Acquired forces a) in x direction, b) in y (radial) direction, and c) in z (feed) direction from simulations using various nose radius and different approach angles for 0.05 mm depth of cut.	39
Figure 4.2. Acquired forces a) in x direction, b) in y (radial) direction, and c) in z (feed) direction from simulations using various nose radius and different approach angles for 0.15 mm depth of cut.	40
Figure 4.3. Acquired forces a) in x direction, b) in y (radial) direction, and c) in z (feed) direction from simulations using various nose radius and different approach angles for 0.25 mm depth of cut.	41
Figure 4.4. Acquired forces a) in x direction, b) in y (radial) direction, and c) in z (feed) direction from simulations using various oblique and rake angles for 0.12 mm depth of cut.	43

Figure 4.5. Acquired forces a) in x direction, b) in y (radial) direction, and c) in z (feed) direction from simulations using various oblique and rake angles for 0.25 mm depth of cut. 43

Figure 4.6. Acquired forces a) in x direction, b) in y (radial) direction, and c) in z (feed) direction from simulations using 14 and 20 degrees of rake angles affecting and without affecting orthogonal data for 0.12 mm depth of cut.44

Figure 4.7. Acquired forces a) in x direction, b) in y (radial) direction, and c) in z (feed) direction from simulations using 14 and 20 degrees of rake angles affecting and without affecting orthogonal data for 0.25 mm depth of cut.45

Figure 4.8. Acquired forces a) in x direction, b) in y (radial) direction, and c) in z (feed) direction from simulations using various feed rates for 0.12 mm and 0.25 mm depths of cut.46

Figure 4.9. a) The fixture used for clamping tool holder on the dynamometer. b) Measuring forces using dynamometer48

Figure 4.10. a) Measuring the surface roughness of the hole using MarSurf. b) Measuring the circularity and cylindricity of the hole using CMM machine.....49

Figure 4.11. a) Measuring the circularity of hole in different height levels. b) measuring the cylindricity of hole by comparing the circularity of circles using CMM machine.....50

Figure 4.12. a) Wear in the nose of tool T-038 b) Wear in the nose of tool T-042 after 10 passes of cut with 0.12 mm depth of cut.....53

List of Tables

Table 2.1. Geometrical and Material properties of miniature boring tools.....	20
Table 2.2. Cutting conditions of validation tests.....	21
Table 3.1. Tool and tool holder’s length and tolerance.	29
Table 3.2. Modal stiffness of different Tool-Holder configurations measured by modal tests.	34
Table 3.3. Parameters used in the verification of boring chatter experiments in [51].	35
Table 4.1. Depth of cut, nose radius and approach angle values used for simulations.....	37
Table 4.2. Cutting tests’ conditions used for simulations.	38
Table 4.3. Depth of cut, oblique and rake angle values used for simulations.....	42
Table 4.4. Cutting tests’ conditions used for simulations.	42
Table 4.5. Cutting test conditions for experiments	47
Table 4.6. Geometrical and material properties of miniature boring tools	48
Table 4.7. Measured forces in 3 directions from experiments using 5 different boring tools.	50
Table 4.8. Measured geometric errors and surface roughness from experiments.....	52
Table 4.9. Measured geometric errors and surface roughness from experiments for worn and sharp tools	53

1. Literature Survey

1.1 Introduction

The precise hole-enlarging process is achieved through boring process, utilizing miniature boring tools with inclined cutting edges, including rake, oblique, approach, and back-approach angles (see Figure 1.1 and Figure 1.2). The main objective is to achieve highly accurate holes in various industries such as aerospace, medical, and military, where minimizing surface roughness and geometric errors is critical. Among various parameters, radial force plays a significant role, causing tool deflection and contributing to chatter, resulting in poor surface roughness and dimensional errors. Therefore, this literature review investigates the mechanics and dynamics of the boring process, including surface roughness, cylindricity, and circularity, in the subsequent sections.

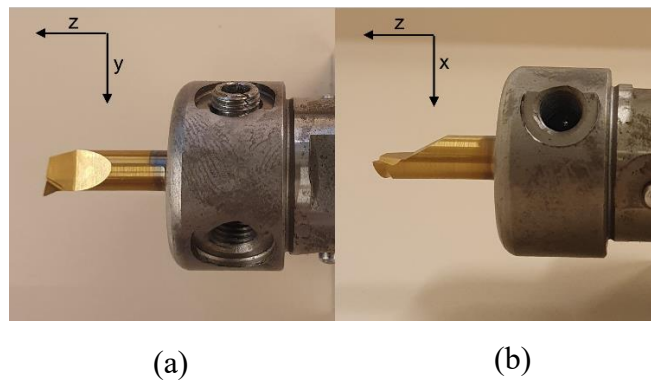


Figure 1.1. a) top and b) side view of a miniature boring tool.

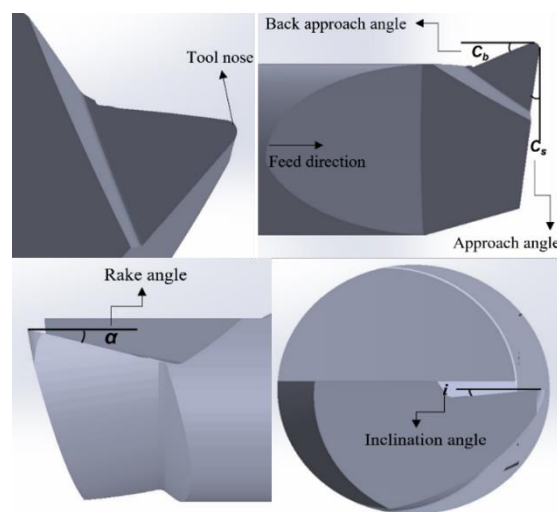


Figure 1.2. Geometric properties of a miniature boring tool.

1.2 Mechanics of Boring Process

A model for the mechanics of the boring process, considering insert geometry and cutting parameters, was provided by Atabey [1]. The total cutting forces for multiple insert boring heads, including runouts, were calculated using the previous model, and the impact of runouts on achieving satisfactory hole surface and dimensional tolerances was investigated [2]. These models have been validated through experiments. In another study, chip geometry was calculated using B-spline interpolation techniques. Additionally, a method for calculating forces in three directions (x-y-z) was proposed, assuming the cutting edge is divided into straight elements. The validation test results, and model outcomes have shown good agreement, with a deviation of 7-10% in cutting force [3].

1.3 Dynamics of Boring Process

One of the most common issues in boring processes is chatter. Researchers have made efforts to understand and model the dynamic behavior of the boring process. A dynamic model of the boring process in the time domain was presented by Lazoglu et al. [4]. An analytical model of chatter stability was introduced, considering precise chip geometry and important cutting angles. This model reduces the stability solution to a 1D equation for the boring process [5]. Moetakef-Imani et al. [6] in this study showed that dynamic simulation of the boring process enables the prediction of cutting forces and vibration frequencies in stable operations, facilitating parameter optimization. The dynamics of the boring bar were modeled to investigate the stiffness over various overhang lengths. However, the dependence of stiffness on tool length, frequency, mass, and clamping unit properties should be considered in more detail and separately [7]. Mei et al. [8] proposed a method to mitigate chatter in the boring process by adding damping to all modes using a controller. In a recent study, an analytical model was developed to predict dynamic cutting forces, incorporating the time-varying tool path [9].

The other case is to detect the chatter during boring process. Mode coupling chatter detection during the boring process was investigated using a PVDF sensor system. The aim was to detect mode coupling chatter occurrence using a simple computational method to measure the torque signal [10]. In the other paper, a new prediction method based on PDEs was proposed to enhance precision in boring deep holes. This method predicts the radial throw of the boring tool spindle and emphasizes the optimization of spindle speed and cutting forces for more precise boring operations [11].

Moreover, researchers have investigated different methods to address and prevent the chatter problem in boring process. One solution is the use of dampers in boring bars, and various types of dampers have been studied over the past three decades. Friction dampers based on Coulomb and viscous frictions were introduced as effective solutions for high vibrating frequencies, offering a simple design and precise boring operation [12]. Another study examined the effect of passive piezoelectric shunt damping on process stability using analytical and finite element models. The results demonstrated that this type of damping can increase the stability limit of the boring process [13].

The need for active damping to maintain the flexibility of long projecting boring tools was demonstrated by Abele et al. [14] and experimental test results showed that this type of damping can improve the surface quality of the workpiece in boring operations. Ramesh et al. [15] explored the effect of double impact dampers on tool wear and cutting temperature, revealing optimum damper positions and cutting conditions through ANOVA analysis.

The use of magnetorheological (MR) fluid-controlled boring bars has been proposed as one of the effective chatter suppression methods. An improved MR fluid-based boring bar was proposed by Mei et al. [16] which allows for various stiffness and damping ratios but lacks independent control. These MR-equipped bars have demonstrated effectiveness at different spindle speeds. However, their FEA analysis showed that adjusting natural and damping frequencies is effective at low spindle speeds but not at high spindle speeds.

In the context of improving dynamic stability of boring process, the effectiveness of semi-active radially arranged magnetorheological (MR) fluid dampers in reducing surface roughness and chatter occurrence has been demonstrated. The adjustable properties of MR fluids, such as magnetic field strength, stiffness, and energy dissipation, make the control of MR-equipped boring bars more convenient [17]. Another work proposed the use of a sliding mode control algorithm in conjunction with use of MR fluids for active damping purpose. This algorithm offers robustness against disturbances [18]. Through FEA methods and experiments, it has been shown that different damper materials can effectively minimize the displacement of boring bars. Copper has been identified as the most proper damping material among various options [19].

Another solution for chatter suppression is the use of tuned mass dampers for boring bars. An optimized tuneable vibration absorber based on spring mass and its stiffness was designed for chatter suppression. Mode summation method has been used for defining the specification of the tuneable vibration absorber [20]. Another study proposed a tuned holder that relies on the approximate natural frequency of the holder matching the natural frequency of the bar. The

addition of a sleeve to the holder made it impossible to adjust the assembly dynamics, resulting in a 69% reduction in magnitude during experiments [21]. A new receptance coupling method was utilized for absorber optimization, enabling parameter optimization using free mass and joining position [22].

Dynamic analysis of boring bars can provide insights into enhancing the boring process precision by reducing chatter occurrence. In a study, the use of high-stiffness carbon fiber epoxy was proposed in the production of a boring bar capable of suppressing chatter. Their advantage would be suppressing the chatter in boring bars with high overhang ratio (length-to-diameter) up to 10:7 [23]. In another study Åkesson et al. [24] modeled the dynamics of boring bars under different clamping conditions using the Multi-span Euler-Bernoulli beam theory. The results showed that the damping ratio and natural frequency of the boring bar can vary under different clamping conditions such as number and size of clamping as well as tightening torque. The effect of a fractional-order model of magnetorheological fluid on vibration control in nonlinear boring bars was investigated using numerical methods for theoretical analysis [25]. Additionally, an automatic tuned mass damper (TMDs) for boring bars was proposed by Altintas et al. [26], which allows for the attachment of different boring heads and enables application in a wide range of length-to-diameter ratios.

Aliakbari et al. [27] investigated the effect of an anti-vibration toolholder on chatter suppression in long boring bars. However, due to material uncertainties and geometrical tolerances, the results of dynamic analysis were not repeatable. Takahashi et al. [28] enhanced the stiffness of boring tools by formulating the dependency of chatter stability on structural dynamics and utilizing an anisotropic structure. FEM analysis confirmed the enhancement of dynamic stiffness. Iklodi et al. [29] showed that one of the issues encountered when using TMDs is displacement constraints during regenerative cutting forces. It also highlighted the impact of collisions in TMDs on system performance and emphasized the importance of preventing collisions in enclosed TMDs.

Hintze et al. [30] proposed the use of tuned mass dampers (TMDs) with small diameter slender boring bars to achieve more accurate and precise boring operations. Analytical, FEM, and experimental investigations confirmed the improvement of the process, with reduced noise amplitudes and improved dynamic compliances when using TMD-equipped slender bars.

In another study, the influence of passive impact dampers and tuned mass dampers on the dynamic stability and surface roughness of the workpiece was investigated through the development of mathematical models. The importance of overhang in utilizing these two types

of dampers was demonstrated, and the results revealed that passive impact dampers (PIDs) are more effective than TMDs in higher length-to-diameter ratios [31].

1.4 Surface Roughness and Geometric Errors in Boring Process

Since hole enlarging process using miniature tools employs to generate precise holes in workpieces, the holes geometric and dimensional precision comes to be very important issue. In this section a literature survey on the effective parameters on the surface roughness and geometric errors of bored holes during hole enlarging process has been provided.

The production of accurate mechanical parts such as engine blocks, hydraulic actuators, and pumps need to be generated by high precision finish boring. Since the precision of cylindrical components has a substantial impact on the final product's performance, their accuracy needs to be measured by cylindricity. The specification of cylindricity tolerance is characterized by a tolerance zone that is limited by two concentric cylinders. It is within this zone that the surface is required to conform. In relation to the engine's power, oil consumption, and piston ring friction, it is vital to recognize the significance of cylindricity, particularly when considering the engine block's cylinder bore [32–35].

The circular and cylindrical characteristics constitute fundamental geometric attributes in machinery. The fitting specifications for cylindrical parts have important implications for the performance of precision products and are determined by size tolerances and geometric anomalies, such as the cylindricity error of the interfacing components [36].

Compensating for machining errors to achieve precise boring operations has been a challenging problem since the beginning. In a study by Gao et al. [37], the utilization of a servo system with piezoelectric actuators was proposed for real-time error compensation in the system of a designed small overhung boring bar. Their results demonstrated a 40% improvement in roundness errors.

A monitoring method has been developed for monitoring tool wear and surface finish quality in deep hole boring operations. This method utilizes the frequency band energy ratio around the natural frequency of the boring bar to monitor surface quality [38].

In another research study, Singh et al. [39] focused on improving surface roughness and flank wear by suppressing chatter during the boring operation using particle-damped boring bars.

Additionally, Sørby [40] introduced a slender boring bar equipped with a strain sensor to absorb vibration and enhance the precision of internal turning operations for boring bars with high overhang ratios (up to 14).

In another study, Lotfi et al. [41] investigated the use of 3D elliptical ultrasonic-assisted boring operations, both numerically and empirically. The analysis results were compared with conventional boring operations, and it was found that employing this method resulted in a reduction in surface microstructure change and the impact of cutting parameters on surface roughness. Furthermore, Ghongade et al. [42] examined the influence of overhang ratio in boring operations on deflection, vibration, and tool wear.

The effect of chucking methods on the roundness error of bored holes was investigated by Kahng et al. [43] using curved-beam theory to analytically model the deformation of the workpiece under various conditions of chucking and using different materials. The test results showed that although increasing the number of chucking points can enhance the roundness error, increasing the chucking force also increases the roundness error. Based on the experimental and FEM simulation results of a finish boring process, Lei et al. [44] demonstrated that workpiece thermal expansion and deformation, caused by cutting and clamping forces, as well as spindle radial error motion, are key factors contributing to the deviation of cylindricity. Although several factors impact the cylindricity of the bored hole, the most significant one is the spindle radial error, which accounts for more than 50% of the cylindricity error.

Korkut et al. [45] conducted several cutting tests with different cutting parameters, boring tool materials, and overhang ratios to find optimized parameters for achieving better circularity of bored holes. The circularity was enhanced at higher depths of cut, while an increase in overhang length at small depths of cut resulted in a higher deviation from circularity in bored holes.

Using machining conditions and considering the kinematic motion deviation of the boring process, a surface roughness simulation model has been developed to predict the surface quality after the boring operation. As a result, this model can predict geometric anomalies for a simple boring process under various cutting conditions and kinematic deviations [46].

Chandrasekhara Sastry et al. [47] investigated the effect of cooling conditions on the cutting temperature, cutting force, workpiece surface roughness, cutting speed, and feed rate during the boring process of a hole using gunmetal as the workpiece material. It was found that cryogenic cooling condition was the most effective in reducing the cutting temperature. Dry cutting condition had the most significant effect on reducing cutting forces and surface roughness. Achieving the hole with minimum geometric errors (circularity and cylindricity) was possible with cryogenic cooling condition. Furthermore, cutting speed played a vital role in determining surface roughness in both dry and wet boring, while feed rate affected surface roughness in cryogenic boring.

In another study [48], the aforementioned parameters were investigated for the boring of HSLA ASTM A36 steel. The experimental results demonstrated a significant reduction in cutting temperature and force during cryogenic boring. Cutting speed was identified as a key factor in determining cutting force in dry, wet, and cryogenic environments. The values of circularity and cylindricity decreased with the transition from dry to wet to cryogenic cutting environments.

1.5 Objective

This thesis aims to investigate the precision of tiny holes generated by miniature boring tools. In the literature survey, numerous analytical, numerical, and empirical models have been developed and proposed to investigate the mechanics and dynamics of boring processes. Most of the dynamic analyses of the boring process have been conducted on long boring bars used for deep hole boring operations, as they tend to cause chatter. These analyses aim to gain a deeper understanding of their dynamics and propose new methods for chatter suppression in long boring bars. However, in this thesis, miniature boring tools are used to enlarge small holes and enhance their precision in terms of surface roughness, circularity, and cylindricity. Therefore, the investigation in this thesis does not focus on the impact of overhang ratio of the boring bars on the chatter problem. Instead, the effect of the geometrical properties of the boring tool and the clamping stiffness of the tool-holder configuration are examined.

Regarding the investigation of the precision of bored holes, it is noted that the literature review explores the effects of various variables such as cutting conditions, cooling environment, and clamping issues on the surface roughness, circularity, and cylindricity of the holes. However, the effect of the geometrical properties of the boring tool edge has not been thoroughly investigated.

The aim of this study is to investigate the effect of the geometrical properties of the tool edge on the precision of the produced small holes. To achieve this, an analytical force model has been developed based on the geometrical properties of the tool edge. The main objective of this model is to optimize the design of miniature boring tools by minimizing the radial force responsible for tool deviation, chatter, and poor surface roughness. Therefore, the force model is utilized to predict the cutting forces accurately during the hole enlarging process using highly accurate chip geometry area.

The study investigates the effect of different geometrical properties on the value of radial forces, and design ideas based on these findings have been communicated to the manufacturer.

An experimental setup for the hole enlarging process using the produced tools has been prepared, and the experimental and simulation results have been analyzed to determine the optimal values for the geometrical parameters of the tool edge, aiming to achieve more precise holes in terms of surface roughness, circularity, and cylindricity.

1.6 Thesis Layout

The thesis is organized as follows:

In Chapter 2, the mechanics of the boring process analysis is provided. An explanation of a precise uncut chip thickness calculation for different tool-workpiece engagements is given, and a force model based on this calculation is proposed. Additionally, an experimental validation section is included at the end of the chapter, where the validation test setup and the comparison of simulation and test results are explained.

Chapter 3 focuses on the dynamic analysis of the boring process. A chatter stability model based on the tool edge geometry is adapted, and an experimental validation test setup is described. The investigation of the clamping stiffness of the tool-holder configuration is discussed through stiffness tests, measured FRF, and modal analysis.

In Chapter 4, a discussion about simulation results is provided, considering different cutting conditions and geometrical properties and their effects on cutting forces. Furthermore, the test results obtained from cutting tests using boring tools produced with different geometrical properties are investigated. Optimum values for the geometrical properties of the boring tool are sought to achieve good geometric accuracy and surface roughness after the hole enlarging process.

In Chapter 5, the contributions of the thesis to the literature, the conclusions and the future work are provided.

2. Mechanics of Boring Process

In this section, a force model for precise hole enlarging processes using miniature boring tools has been proposed. The model is based on the oblique transformation and includes the nose radius effect on the cutting forces. This force model uses a more precise computation of the chip area, which leads to estimations of the cutting force that are more accurate. Additionally, it proposes different configurations for the chip area based on negative and positive approach angles. However, the model does not take into account the effect of the hone radius and its impact on edge forces, as well as the variation of edge forces along the nose radius. The modeling of edge forces based on hone radius is not yet complete for this operation, despite the fact that it is known that increasing the hone radius will increase the edge forces and consequently the total forces; In the future, more study will be done to incorporate edge force modeling of miniature boring tools.

Since the depth of cut and feed rate values in precise hole enlarging processes are small, the tool nose and its geometric properties play a crucial role in determining the cutting force amounts. The model has been developed based on these geometric parameters and can be used to predict cutting forces for the boring process using various miniature boring tools with different geometric properties. To study the effect of geometric properties of the cutting edge on the cutting forces, a precise chip area has been calculated using the proposed model. Then, by using orthogonal data for a specific material and applying the oblique transformation, cutting forces have been calculated. A validation test setup using miniature boring tools has been prepared, and the model has been verified using the test results.

Depth of cut (b), nose radius (r), oblique angle (i), rake angle (α), approach angle (C_s), and feed rate (f) are values define the precise hole enlarging process.

2.1 Kinematics of Boring Process

The precise hole-enlarging process is a boring process in which the tool used is a miniature boring tool. Miniature boring tools are tools with inclined cutting edges that consist of rake, oblique, approach, and back-approach angles (see Figure 2.1). In the precise boring process, the tool follows a linear path along the interior hole of the workpiece (z-axis), while the workpiece rotates on the spindle of the lathe machine (see Figure 2.2).

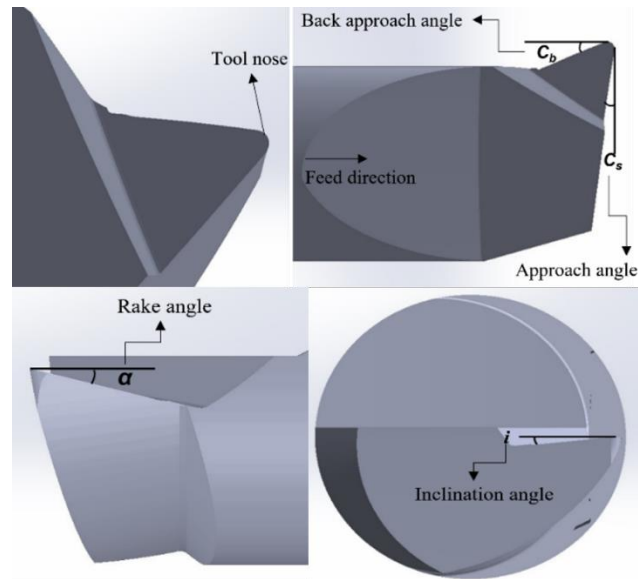


Figure 2.1. Geometric properties of a miniature boring tool.

As can be seen from Figure 2.2, the tangential, radial, and feed forces act in the x, y, and z directions respectively. Since it is a precise machining process and the final quality of the hole is of utmost importance, the cutting forces, particularly the radial force, play a crucial role (see Figure 2.3).

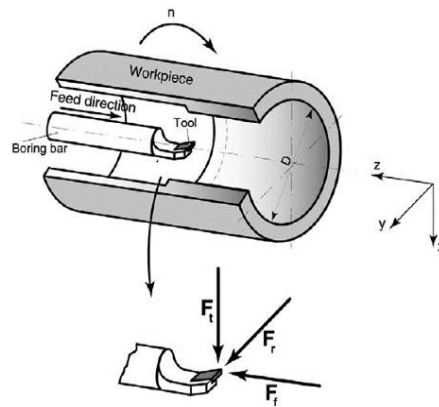


Figure 2.2. Schematic of boring process by Atabey [1]

Consequently, when modeling the cutting forces based on chip geometry, calculating the precise chip area becomes crucial. This section explains the uncut chip geometry and the kinematics of the process, which will be utilized for the development of the force model.

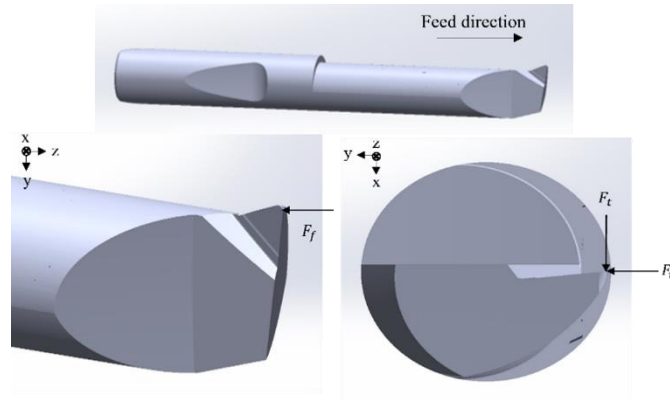


Figure 2.3. Tangential, radial, and feed forces (F_t , F_r , F_f) acting on the tool tip.

The workpiece rotates at a spindle speed of n (rev/min), and the tool moves along the z -axis with a constant feed rate of f (mm/rev). As a result, during each revolution, the tool removes unwanted material, creating a chip whose geometry is affected by the depth of cut, feed rate, nose radius, and cutting tool angles (see Figure 2.4).

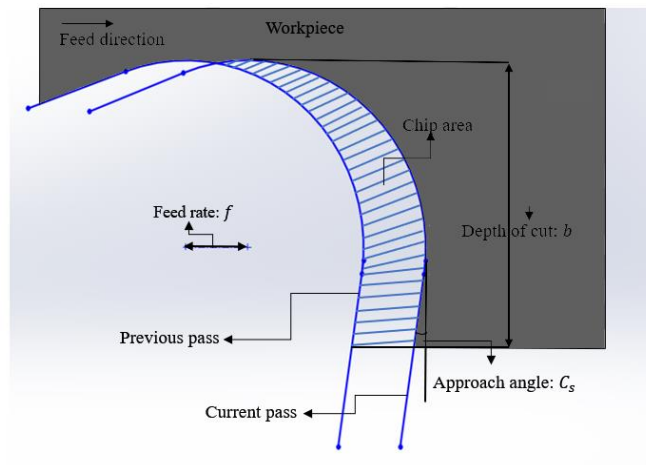


Figure 2.4. The uncut chip area in boring process using a miniature boring tool.

2.2 Modeling of Chip Geometry

Due to the presence of a nose radius, the chip thickness varies along the curved edge of tool, thereby adding complexity to the overall geometry. Furthermore, the cutting tool's angles undergo changes throughout the nose region of the tool.

The combination of parameters such as the depth of cut, feed rate, nose radius values, and approach angle gives rise to different configurations for the tool and workpiece engagements. Consequently, these variations in engagement lead to different chip geometries (refer to Figure 2.5).

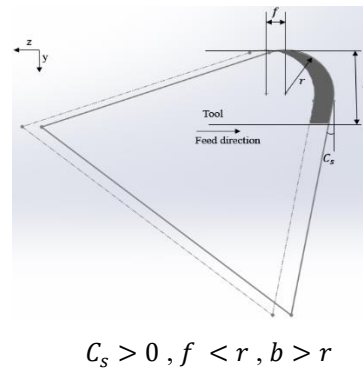
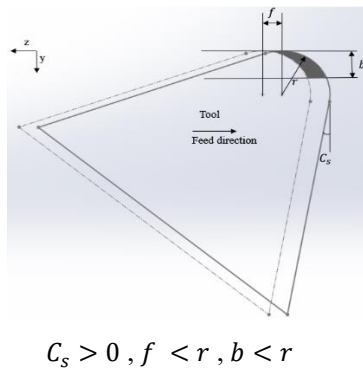
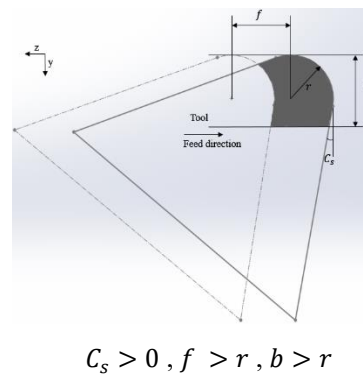
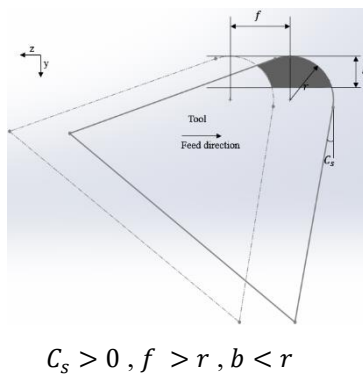
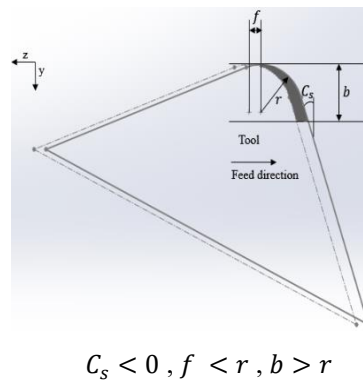
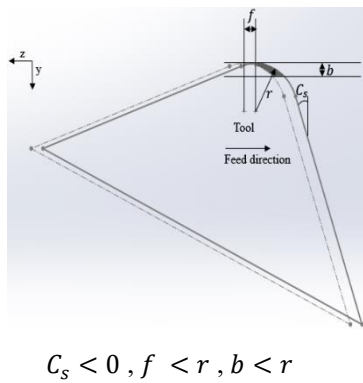
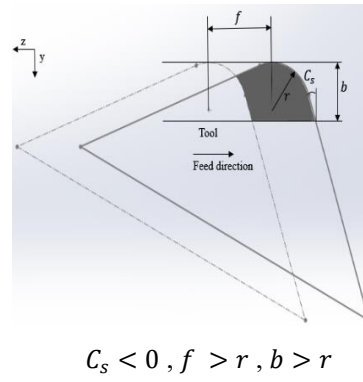
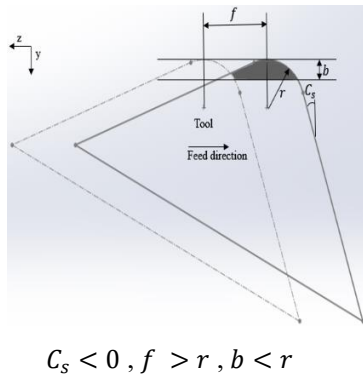


Figure 2.5. Illustration of eight different uncut chip area configurations defined with approach angle (C_s), depth of cut (b), feed rate (f), and nose radius of the tool (r).

The scallops on the workpiece, which are marks left by the feed rate, result in poor surface quality (see Figure 2.6) also it is crucial to maintain high precision in this type of boring

operation using a miniature boring tool. Therefore, it is necessary to employ small values for the feed rate to prevent these issues.

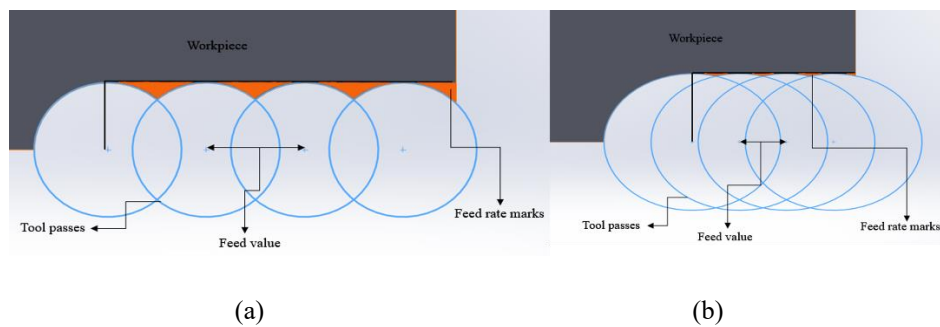


Figure 2.6. Scallop marks left on the workpiece in successive passes due to feed rate a) bigger than nose radius
b) smaller than nose radius.

Considering the practical geometric characteristics of miniature boring tools and the requirement for small feed rate values, two configurations from the aforementioned options have been selected to explain the chip geometry modeling (see Figure 2.7). As depicted in Figure 2.7, the chip geometry has been divided into four sections based on the geometric properties of tool nose and directions of the cutting forces.

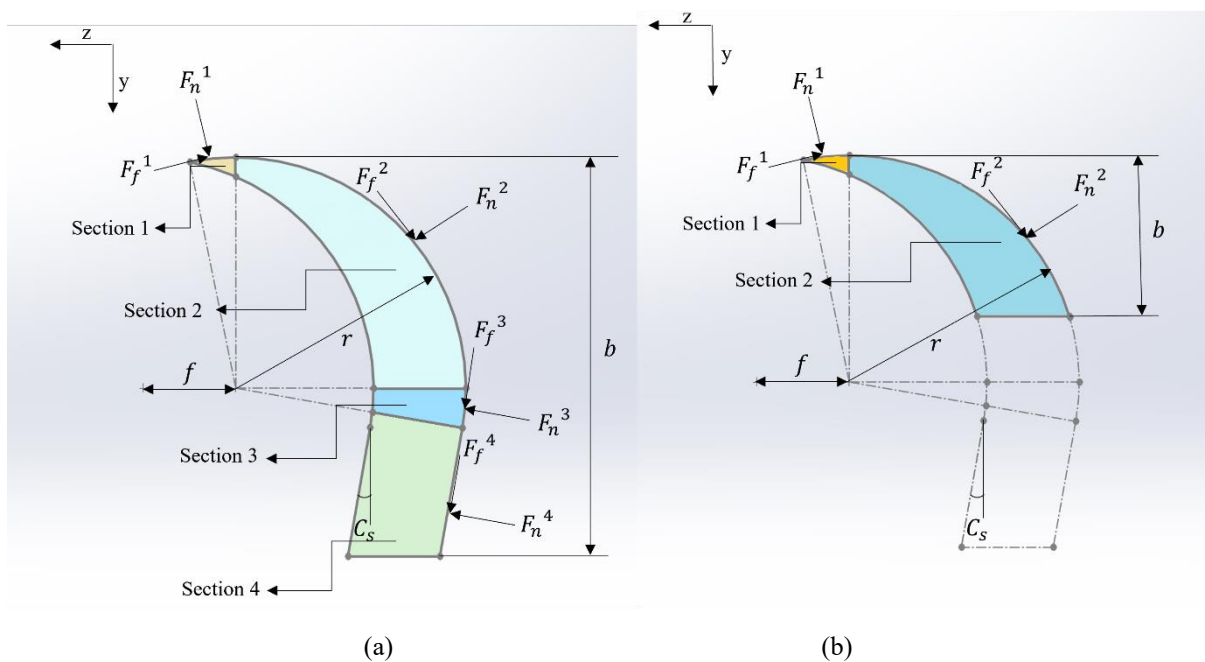


Figure 2.7. Normal and friction forces acting on the uncut chip area when a) $C_s > 0$, $f < r$, $b > r$ b) $C_s > 0$,
 $f < r$, $b < r$

Each section has been further subdivided into smaller elements with slight variations but following the same logical approach. Each of these elements is considered as a cutting edge, and the objective is to calculate the cut chip thickness for each of them (see Figure 2.8). To

accurately model the chip area, we have utilized the proposed model by Altintas [49] and made appropriate adaptations.

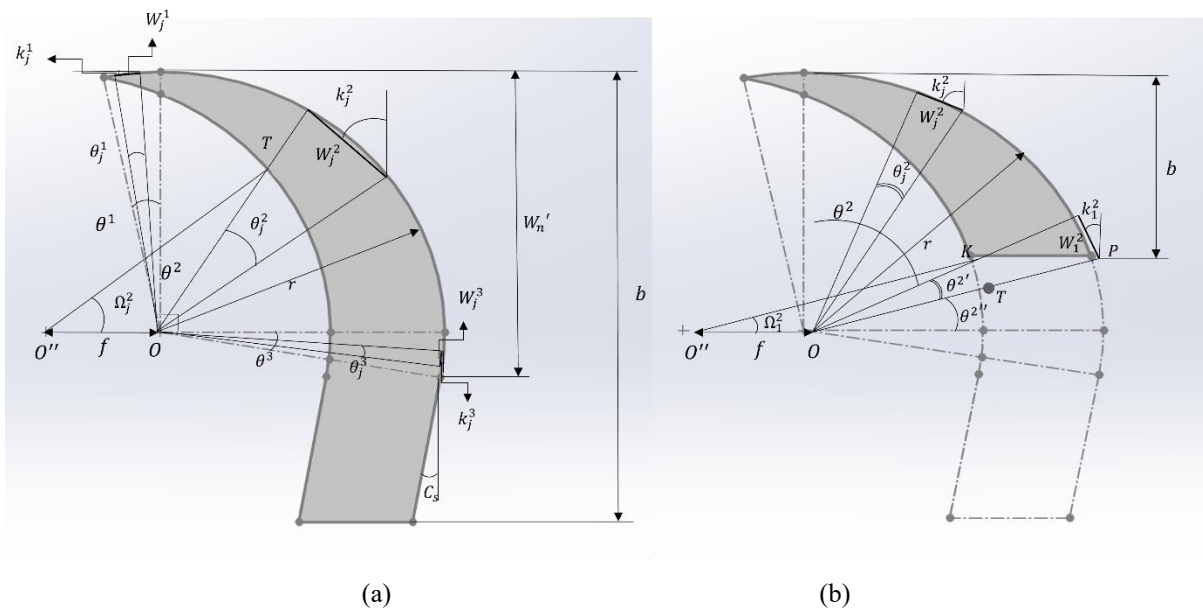


Figure 2.8. division of the uncut chip area into elements when a) $C_s > 0, f < r, b > r$ b) $C_s > 0, f < r, b < r$

2.3 Depth of Cut higher than Nose Radius

The first configuration for the uncut chip area occurs when the depth of cut is higher than the nose radius: In this case, the proportional engagement of the tool and workpiece results in all four sections being cut. Each of these sections is then subdivided into smaller elements, enabling the calculation of the elemental chip thickness in each segment.

2.3.1 Elemental chip thickness for section 1

Section 1 is the region that is formed by the contact points of the new and previous passes at the top of the nose (see Figure 2.8).

For calculating the elemental chip area following elemental values are needed and calculated by 2.1-2.6):

$$\theta^1 = \frac{\pi}{2} - \cos^{-1}\left(\frac{f}{2r}\right), \theta_j^1 = \frac{\theta^1}{j^1} \quad 2.1$$

$$A^1 = \sum_1^{j^1} A_j^1, A_j^1 \approx A_j^{1'} - A_j^{1''} \quad 2.2$$

$$A_j^{1'} = \left(\frac{1}{2}\theta_j^1 r^2\right), A_j^{1''} = A_{OTT'} = \left(\frac{1}{2}TO_j^1 TO_{j+1}^1 \sin(\theta_j^1)\right) \quad 2.3$$

$$TO_j^1 = \sqrt{f^2 + r^2 - (2fr \cos(\Omega_j^1))} \quad 2.4$$

$$\frac{\overline{OO''}}{\sin\left(\pi - \left(\frac{\pi}{2} - (\theta_j^1(j^1 - 1))\right) + \Omega_j^1\right)} = \frac{\overline{TO''}}{\sin\left(\pi - \left(\frac{\pi}{2} - (\theta_j^1(j^1 - 1))\right)\right)} \quad 2.5$$

$$\Omega_j^1 = \frac{\pi}{2} + (\theta_j^1(j^1 - 1)) - \sin^{-1}\left(\frac{f}{r} \sin\left(\frac{\pi}{2} - (\theta_j^1(j^1 - 1))\right)\right) \quad 2.6$$

where θ^1 , j^1 , f , and r are total arc angle for section 1, number of elements for section 1, feed rate, and nose radius respectively. A_j^1 is the elemental chip area of section 1. To calculate the elemental chip area, first, the area of the circle's arc has to be calculated. The area of OTT' can be calculated by approximating it as a triangle. Then, the elemental area will be the difference between them.

2.3.2 Elemental chip thickness for section 2 and 3

For the chip area calculation of sections 2 and 3, the same procedure has to be followed. However, the difference lies in the total angle of the arc. In section 2, the total angle is 90 degrees since it represents a quarter of a circle. In section 3 (refer to Figure 2.8), the total angle is equal to the tool's approach angle. For further calculations see Appendix.

$$\left\{ \begin{array}{l} \theta^2 = \frac{\pi}{2} \\ \theta_j^2 = \frac{\theta^2}{j^2} \\ A^2 = \sum_1^{j^2} A_j^2 \end{array} \right. \quad 2.7$$

and for section 3 the equations will change as below:

$$\left\{ \begin{array}{l} \theta^3 = C \\ \theta_j^3 = \frac{\theta^3}{j^3} \\ A^3 = \sum_1^{j^3} A_j^3 \end{array} \right. \quad 2.8$$

2.3.3 Elemental chip thickness for section 4

This section can be considered as a straight cutting edge (refer to Figure 2.8), so there is no need to divide it into smaller elements.

$$W'_n = r + r \sin C \quad 2.9$$

$$A^4 = A^{4'} + A^{4''} \quad 2.10$$

$$A^{4'} = bf - W'_n f, A^{4''} = (TO_{j2}^2) \sin(C) \quad 2.11$$

where A^4 , $A^{4'}$, and $A^{4''}$ represent the total area of section 4, the area of the rectangular section, and the area of the triangular section, respectively. Section 4'' has a tiny rounded edge that can be considered almost a triangle. r denotes the nose radius, while C and f represent the approach angle and the feed rate value, respectively.

2.3.4 Elemental Angles of each Section

Due to presence of nose radius, rake, oblique and approach angles change along the curved shaped of the cutting edge (see Figure 2.9).

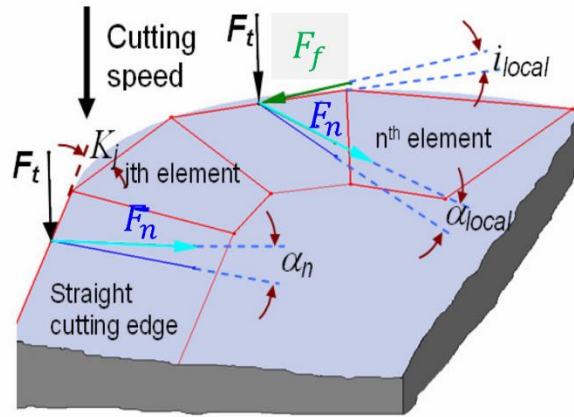


Figure 2.9. 3D representation of the local cutting angles on the insert [50].

The elemental angles are calculated by Eq. (2.12-2.15)

$$\begin{cases} W_{ji}^i = 2r \left(\sin \left(\frac{\theta_{ji}^i}{2} \right) \right) & i = 1, 2, 3 \\ W_{ji}^i = b - W'_n & i = 4 \end{cases} \quad 2.12$$

$$\begin{cases} k_{ji}^i = \sin^{-1} \left(r \cos(\theta_j^i (j^i - 1)) - \cos(\theta_j^i j^i) \right) / W_{ji}^i & i = 1, 2, 3 \\ k_{ji}^i = C & i = 4 \end{cases} \quad 2.13$$

$$\begin{cases} \alpha_{ji}^i = \sin^{-1}(\sin(k_{ji}^i) \sin(\alpha_n) + \cos(k_{ji}^i) \sin(i)) & i = 1 \\ \alpha_{ji}^i = \sin^{-1}(\cos(k_{ji}^i) \sin(\alpha_n) + \sin(k_{ji}^i) \sin(i)) & i = 2, 3 \\ \alpha_{ji}^i = \alpha_n & i = 4 \end{cases} \quad 2.14$$

$$\begin{cases} i_{ji}^i = \sin^{-1}(\cos(k_{ji}^i) \sin(\alpha_n) + \sin(k_{ji}^i) \sin(i)) & i = 1 \\ i_{ji}^i = \sin^{-1}(\sin(k_{ji}^i) \sin(\alpha_n) + \cos(k_{ji}^i) \sin(i)) & i = 2, 3 \\ i_{ji}^i = i & i = 4 \end{cases} \quad 2.15$$

where W_{ji}^i denotes the elemental depth of cut, k_{ji}^i denotes the elemental approach angle, α_{ji}^i denotes the elemental rake angle and i_{ji}^i denotes the elemental inclination angle for each section. α_n and i represent the normal rake angle and the inclination angle respectively.

The second configuration is when the depth of cut is smaller than nose radius: When depth of cut is smaller than nose radius just the section 1 and a segment of the section 2 are in cut, therefore the calculation of chip area in section 2 is a little bit more complex geometrically (see Figure 2.8.(b)).

2.4 Depth of Cut smaller than Nose Radius

The second configuration occurs when the depth of cut is smaller than the nose radius. In such a scenario, just section 1 and a portion of section 2 are involved in the cutting process. As a result, the computation of the chip area in section 2 becomes somewhat more complex from a geometrical perspective.

2.4.1 Elemental chip thickness for section 1

The calculation of the chip area in section 1 remains the same as in the previous scenario.

$$\begin{cases} \theta^1 = \frac{\pi}{2} - \cos^{-1}\left(\frac{f}{2r}\right) \\ \theta_j^1 = \frac{\theta^1}{j^1} \\ A^1 = \sum_1^{j^1} A_j^1 \end{cases} \quad 2.16$$

2.4.2 Elemental chip thickness for section 2

The logic for calculating the elemental chip thickness remains the same as before, but there is a distinction in the calculation of the area for the first element compared to the other elements.

Area calculation for the first element and other elements are provided in Eq. 2.17 and Eq. 2.18 respectively. Detailed elemental area calculation is provided in Appendix.

$$A_1^2 = A_1^{2'} - A_1^{2''} \quad j = 1 \quad 2.17$$

$$\left\{ \begin{array}{l} \theta^2 = \frac{\pi}{2} - (\theta^{2'} + \theta^{2''}) \\ \theta_j^2 = \frac{\theta^2}{(j^2 - 1)} \\ A^2 = \sum_1^{j^2} A_j^2 \end{array} \right. \quad j = 2, 3, \dots, j^2 \quad 2.18$$

2.4.3 Elemental Angles of each Section

Again, the elemental angles are calculated using Eq. (2.192.22):

$$\left\{ \begin{array}{l} W_{ji}^i = 2r \left(\sin \left(\frac{\theta_{ji}^i}{2} \right) \right) \quad i = 1, 2 \quad j^2 \neq 1 \\ W_{ji}^i = 2r \left(\sin \left(\theta^{i'} / 2 \right) \right) \quad i = 2 \quad j^2 = 1 \end{array} \right. \quad 2.19$$

$$\left\{ \begin{array}{l} k_{ji}^i = \sin^{-1} \left(r \cos(\theta_j^i (j^i - 1)) - \cos(\theta_j^i j^i) \right) / W_{ji}^i \quad i = 1 \\ k_{ji}^i = \sin^{-1} \left(r \cos \left((\theta^{i'} + \theta^{i''}) + \theta_j^i (j^i - 1) \right) - \cos \left((\theta^{i'} + \theta^{i''}) + \theta_j^i j^i \right) \right) / W_{ji}^i \quad i = 2 \quad j^2 \neq 1 \\ k_{ji}^i = \sin^{-1} \left(r \cos(\theta^{i''}) - \cos(\theta^{i'} + \theta^{i''}) \right) / W_{ji}^i \quad i = 2 \quad j^2 = 1 \end{array} \right. \quad 2.20$$

$$\left\{ \begin{array}{l} \alpha_{ji}^i = \sin^{-1} \left(\sin(k_{ji}^i) \sin(\alpha_n) + \cos(k_{ji}^i) \sin(i) \right) \quad i = 1 \\ \alpha_{ji}^i = \sin^{-1} \left(\cos(k_{ji}^i) \sin(\alpha_n) + \sin(k_{ji}^i) \sin(i) \right) \quad i = 2 \end{array} \right. \quad 2.21$$

$$\left\{ \begin{array}{l} i_{ji}^i = \sin^{-1} \left(\cos(k_{ji}^i) \sin(\alpha_n) + \sin(k_{ji}^i) \sin(i) \right) \quad i = 1 \\ i_{ji}^i = \sin^{-1} \left(\sin(k_{ji}^i) \sin(\alpha_n) + \cos(k_{ji}^i) \sin(i) \right) \quad i = 2 \end{array} \right. \quad 2.22$$

2.5 Cutting Forces

Since each small element is considered as a cutting edge, the cutting forces are calculated for each of them, and the summation of these forces will give the total force.

After calculating the elemental chip thickness, depth of cut, and cutting angles, the cutting force coefficients need to be calculated for the calculation of cutting forces. In this model, formulas for the oblique transformation of orthogonal data have been used. However, it is necessary to calculate elemental cutting force coefficients.

To maintain the continuity of the chip, the shear angle has been assumed to be the same for all elements. Additionally, the same chip flow angle, which is equal to the global oblique angle, has been used for all elemental calculations.

$$\left\{ \begin{array}{l} K_{tcj}^i = \frac{\tau(\cos(\beta_n - \alpha_j^i) + \tan i_j^i \tan \eta_c \sin \beta_n)}{\sin \varphi_n \sqrt{\cos^2(\varphi_n + \beta_n - \alpha_j^i) + (\tan^2 \eta_c \sin^2 \beta_n)}} \quad i = 1, 2, 3, 4 \\ K_{ncj}^i = \frac{\tau \sin(\beta_n - \alpha_j^i)}{\cos i_j^i \sin \varphi_n \sqrt{\cos^2(\varphi_n + \beta_n - \alpha_j^i) + (\tan^2 \eta_c \sin^2 \beta_n)}} \quad i = 1, 2, 3, 4 \\ K_{fcj}^i = \frac{\tau(\cos(\beta_n - \alpha_j^i) \tan i_j^i - \tan \eta_c \sin \beta_n)}{\sin \varphi_n \sqrt{\cos^2(\varphi_n + \beta_n - \alpha_j^i) + (\tan^2 \eta_c \sin^2 \beta_n)}} \quad i = 1, 2, 3, 4 \end{array} \right. \quad 2.23$$

After calculating the elemental cutting force coefficients, the elemental cutting forces can be obtained. Although summing these elemental forces will result in total forces, there is a need to convert these forces to the machine coordinates (x, y, z) by utilizing the elemental approach angle using Eq. (2.25) before summing them up.

$$\left\{ \begin{array}{l} F_{tcj}^i = K_{tcj}^i A_j^i \quad i = 1, 2, 3, 4 \\ F_{ncj}^i = K_{ncj}^i A_j^i \quad i = 1, 2, 3, 4 \\ F_{fcj}^i = K_{fcj}^i A_j^i \quad i = 1, 2, 3, 4 \end{array} \right. \quad 2.24$$

$$\left\{ \begin{array}{l} F_x = \sum F_{tcj}^i \quad i = 1, 2, 3, 4 \\ F_y = \sum F_{ncj}^i \sin k_j^i + F_{fcj}^i \cos k_j^i \quad i = 1, 2, 3, 4 \\ F_z = \sum F_{ncj}^i \cos k_j^i + F_{fcj}^i \sin k_j^i \quad i = 1, 2, 3, 4 \end{array} \right. \quad 2.25$$

2.6 Solution Procedure

For the proposed model, the first step involves calculating orthogonal data based on the workpiece material. Then, based on the engagement of the tool and workpiece, the active sections of the chip geometry are determined. Subsequently, the equivalent cutting angles are calculated through oblique transformation for each section.

Equations (2.1-2.22) are used to calculate the elemental chip thickness and cutting angles for each section of the chip area. The chip flow angle is assumed to be equal to the oblique angle for all elements. By utilizing the calculated elemental cutting force coefficients, the elemental cutting forces can be determined in the tangential, normal, and friction directions for each section.

The calculation of the elemental approach angle for each active section is necessary and is based on the elemental depth of cut. These elemental approach angles are then used to convert the elemental cutting forces in the tangential, normal, and friction directions into the elemental forces in the tangential (x), radial (y), and feed (z) directions.

Using Eq. (2.23-2.25) the summation of these forces in each section yields the total forces for that section. Finally, by summing up the forces from all active sections, the total cutting forces for the boring process can be obtained.

2.7 Experimental Verifications:

Cutting tests were conducted using miniature boring tools on the MORI SEIKI NL1500 lathe machine, with AISI 1050 and Ti-6Al-4v selected as the workpiece materials. The utilized tools had a 14° rake angle, 6° oblique angle, and a 0.2 mm nose radius. The other geometric parameters of the tools can be found in Table 2.1.

Table 2.1. Geometrical and Material properties of miniature boring tools

Tool code	Material	Coating	Rake angle (degree)	Oblique angle (degree)	Clearance angle (degree)	Approach angle (degree)	Nose radius (mm)	Honing time (min)
T-038	TC402	TiN	14	6	10	8	0.2	3

The tests were performed at a cutting speed of 110 m/min and a feed rate of 0.03 mm/rev. Two different depths of cut were used, one smaller and the other larger than the nose radius, to validate the proposed model. The cutting conditions are shown in Table 2.2.

Table 2.2. Cutting conditions of validation tests

Material	Cooling condition	Cutting Speed (m/min)	Feed Rate (mm/rev)	Depth of Cut (mm)
1050 Steel	Dry machining	110	0.03	0.12, 0.25
Ti-6Al-4v	Dry machining	60	0.03	0.12, 0.25

To measure the cutting forces, a Kistler micro dynamometer was employed. Due to cylindrical shape of the tool holder, a fixture was required to clamp the tool holder onto the dynamometer (see Figure 2.10).

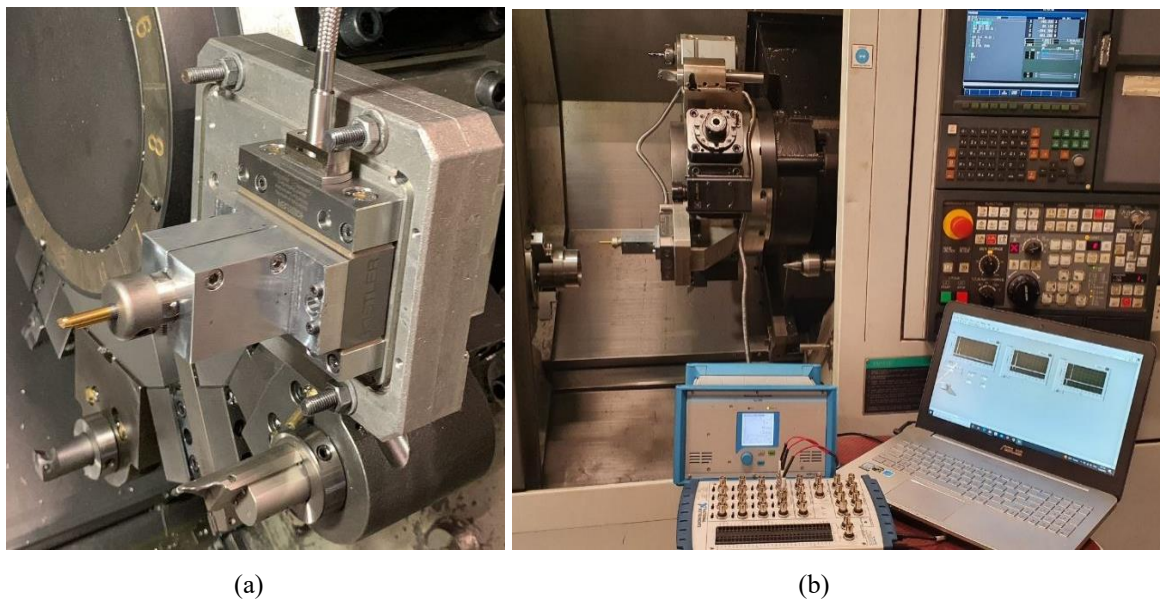
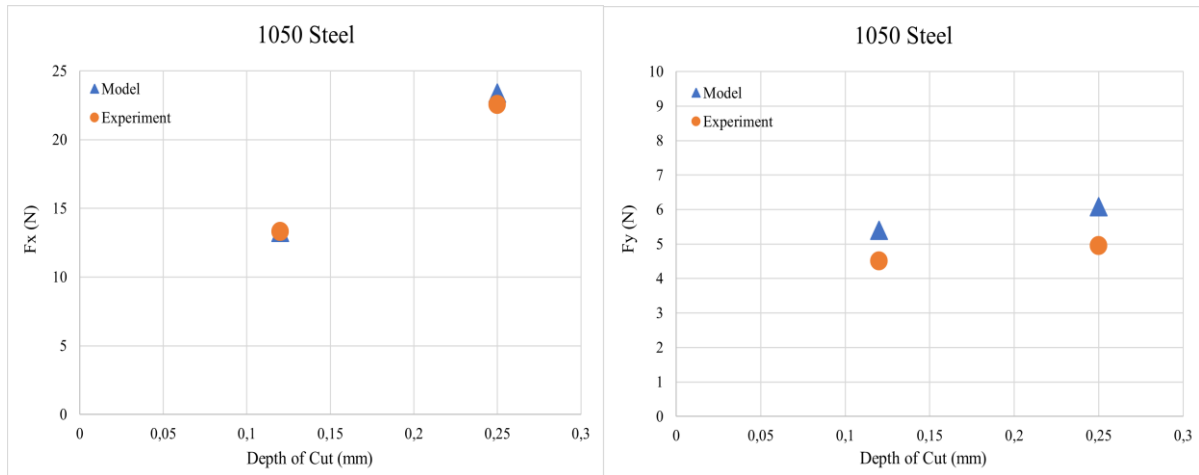


Figure 2.10. a) The fixture used for clamping tool holder on the dynamometer. b) Measuring forces using dynamometer

The proposed force model for boring process was developed as a simulation code, and for verification of the proposed model, simulations were conducted. In the simulations, the edge force coefficients (K_{te} , K_{ne} , K_{fe}) for the tangential, normal, and friction forces were incorporated. These coefficients were determined from previous cutting tests conducted for each material (orthogonal data).

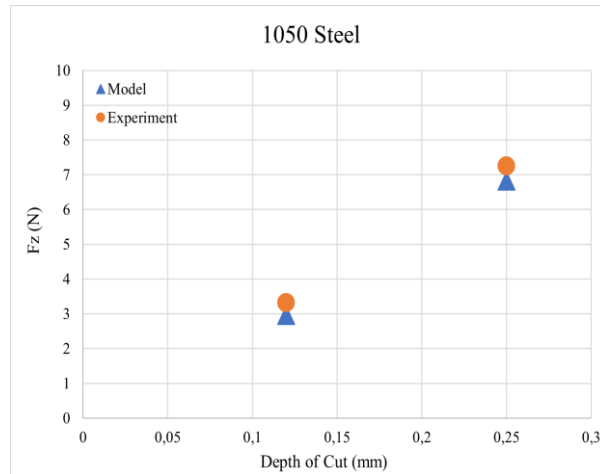
The model predictions and experimental results for different verification tests are presented in Figure 2.11 and Figure 2.12. In the first case, the selected workpiece material was 1050 Steel, and cutting tests were conducted at two depths of cut: one smaller than the nose radius (0.12 mm) and the other larger than the nose radius (0.25 mm) (see Figure 2.11). In the second case, the cutting conditions remained the same, but the workpiece material was changed to Ti-6Al-

4V (see Figure 2.12). As observed from the results, the predicted and measured force values exhibit good agreement.



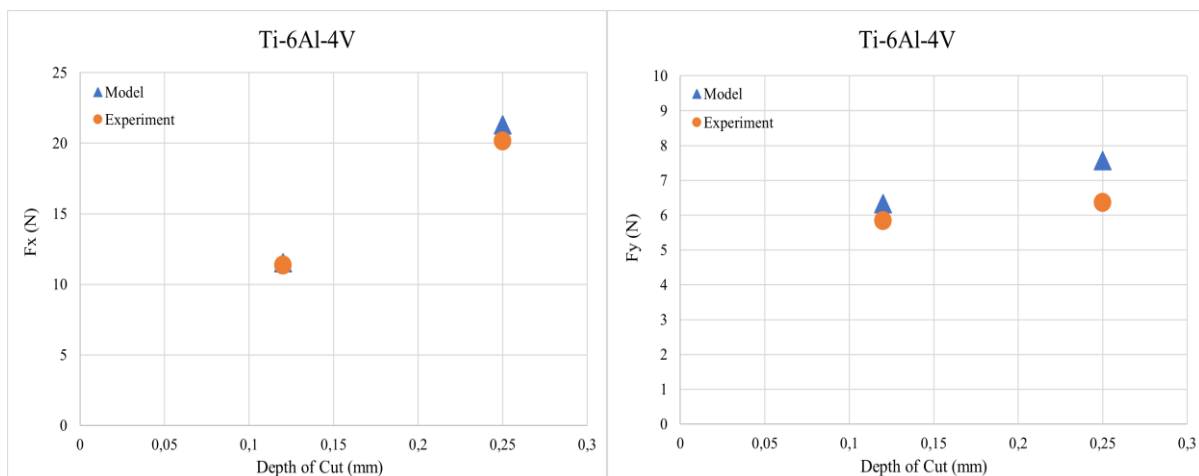
(a)

(b)



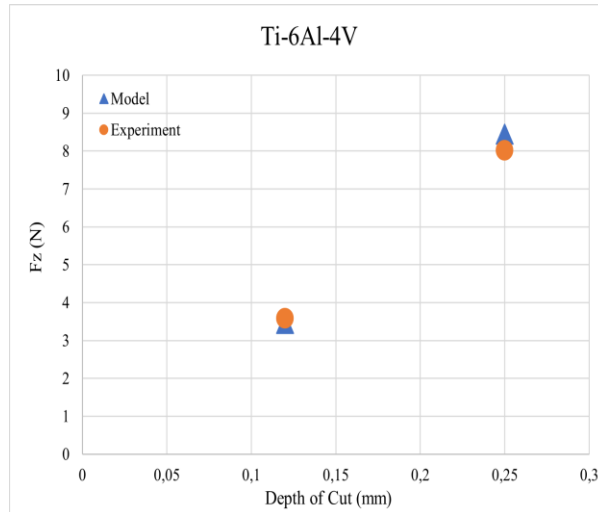
(c)

Figure 2.11. The simulations and experimental results for 1050 Steel workpiece material in a) tangential (x), b) radial (y), and c) feed (z) directions



(a)

(b)



(c)

Figure 2.12. The simulations and experimental results for Ti-6Al-4V workpiece material in a) tangential (x), b) radial (y), and c) feed (z) directions

3. Dynamics of Boring Process

In this chapter, a stability model for the hole enlarging operation using miniature boring tools was adapted from Budak et al. [51]. The model proposed in their study is based on dynamic chip thickness and cutting forces. Additionally, the proposed model includes the nose radius and the negative approach angle effect of inserts. However, since the most commonly used approach angles in the production of miniature boring tools are positive values, our adapted stability model investigates the effect of positive approach angles, in addition to negative and zero approach angles.

Depth of cut (b), nose radius (r), oblique angle (i), rake angle (α), approach angle (C_s), and feed rate (f) are values define the precise hole enlarging process.

3.1 Analytical Modeling of Chatter Stability in Boring Process

In this chapter, the chatter stability model proposed in [51] for the boring process was adapted to include positive approach angles. The hole enlarging process using miniature boring tools is a highly precise machining operation, with very small values for the depth of cut and feed rate. Additionally, the ratio of the depth of cut to the nose radius and the approach angle greatly impact the modeling of chatter stability.

As mentioned in section 2.2, the combination of parameters such as the depth of cut, feed rate, nose radius values, and approach angle gives rise to different configurations for the tool and workpiece engagements (refer to Figure 2.5).

The previously proposed model considered chatter stability for tools with negative approach angles. However, this study proposes a chatter stability model for positive values of approach angles, which are more commonly used in the hole enlarging process. Therefore, this section investigates the modeling of chatter stability for configurations with positive approach angles. Moreover, the reduced 1D eigenvalue problem is utilized to formulate the stability model for this process.

3.1.1 Dynamic Chip Thickness and Cutting Forces

Modeling the dynamic cutting forces is based on dynamic chip thickness; thus, formulating the dynamic chip thickness is the first step in the development of the stability model. Dynamic chip thickness is generated due to the vibration of the tool and workpiece

during the hole-enlarging process. Since the dynamic displacement in the x-direction does not affect the dynamic chip thickness, it can be formulated as a 2D problem.

For this configuration of dynamic chip thickness, resulting from the change in the direction of cutting forces, the dynamic chip thickness is divided into three sections. By observing Figure 3.1, one can deduce that the dynamic chip thickness formulation for section 1 is different from the formulation for sections 2 and 3.

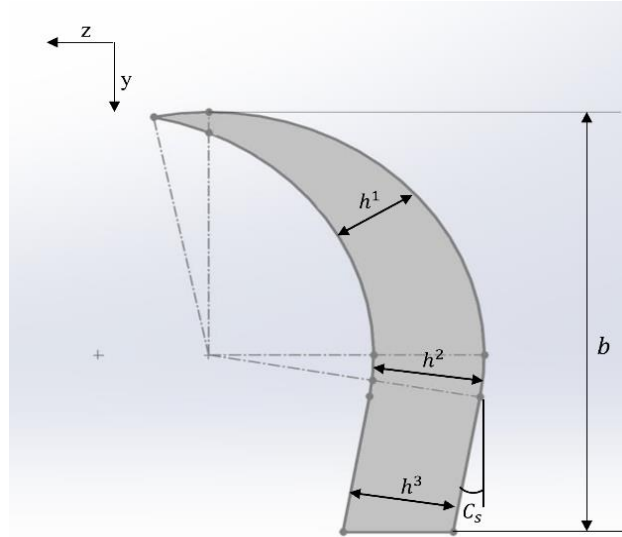


Figure 3.1. Direction variation of dynamic chip thickness of section 1, 2, and 3.

The dynamic chip thickness formulation is provided in Eq. 3.1:

$$\begin{cases} h_m^i(t) = f \cos C_s + (Z_c(t) - Z_w(t) - Z_c(t - \tau) + Z_w(t - \tau)) \cos C_s & i = 1 \\ \quad + (Y_c(t) - Y_w(t) - Y_c(t - \tau) + Y_w(t - \tau)) \sin C_s & \\ h_m^i(t) = f \cos C_s + (Z_c(t) - Z_w(t) - Z_c(t - \tau) + Z_w(t - \tau)) \cos C_s + & i = 2, \\ \quad (Y_c(t) - Y_w(t) - Y_c(t - \tau) + Y_w(t - \tau)) \sin C_s & \end{cases} \quad 3.1$$

where the variable f is utilized to denote the feed per revolution. Moreover, the dynamic displacements of the cutter and workpiece for the current pass are represented by $Z_c(t)$, $Z_w(t)$ and $Y_c(t)$, $Y_w(t)$ respectively. In addition, the respective dynamic displacements of the cutter and workpiece for the previous pass in the z and y directions are denoted by $Z_c(t - \tau)$, $Z_w(t - \tau)$ and $Y_c(t - \tau)$, $Y_w(t - \tau)$. The delay term, denoted by τ , is equivalent to the spindle revolution period in seconds. It is noteworthy that the feed term in Equation 3.1 signifies the static component of the chip thickness. Since this static chip thickness does not have any impact on the regeneration mechanism of chatter problem, it can be ignored in the context of stability analysis.

Therefore, the dynamic chip thickness in turning can be defined as follows:

$$\begin{cases} h_t^i = -\Delta Z \cos C_s - \Delta Y \sin C_s & i = 1 \\ h_t^i = -\Delta Z \cos C_s + \Delta Y \sin C_s & i = 2,3 \end{cases} \quad 3.2$$

where:

$$\begin{aligned} \Delta Z &= (Z_c(t) - Z_w(t) - Z_c(t - \tau) + Z_w(t - \tau)) \\ \Delta Y &= (Y_c(t) - Y_w(t) - Y_c(t - \tau) + Y_w(t - \tau)) \end{aligned} \quad 3.3$$

3.1.1 Effect of Nose Radius and Positive Approach angle

In most hole enlarging processes, the depth of cut utilized is smaller than or at least equal to the nose radius. Consequently, the stable depth of cuts in boring is comparable to the insert's nose radius, making the effect of the insert nose radius critical. Therefore, the stability model must incorporate the tool nose effect. Additionally, miniature boring tools are produced with a positive approach angle, which causes the forces to differ in terms of direction along the curved shape of the tool nose.

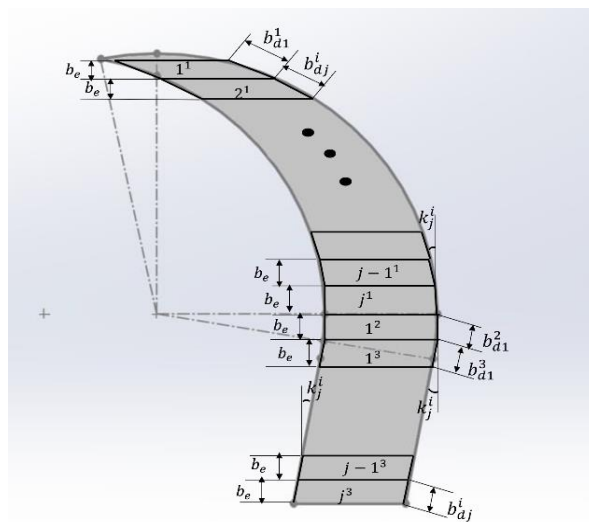


Figure 3.2. Division of chip thickness by trapezoidal elements

As mentioned before, the chip area is divided into three sections, and each section is further subdivided into small elements with a constant elemental depth of cut (see Figure 3.2). The required parameters are then calculated based on the elemental depth of cut.

The elemental values can be defined as follows:

$$\begin{cases} b_j^i = \frac{r}{j^1} & i = 1 \\ b_j^i = b_j^1 = \frac{r \sin C_s}{j^2} & i = 2,3 \end{cases} \quad 3.4$$

$$b_{dj}^i = b_j^i / \cos k_j^i \quad 3.5$$

$$\begin{cases} k_j^i = \frac{\pi}{2} - \tan^{-1} \left(\frac{b_j^i}{S_j^i} \right) & i = 1,2 \\ k_j^i = C_s & i = 3 \end{cases} \quad 3.6$$

$$S_j^i = \sqrt{r^2 - \left(r - \frac{j^i}{n^i} (r - r \sin C_s) \right)^2} - \sum_{j^i}^{n^i-1} S_{j^i} \quad 3.7$$

where b_j^i represents elemental depth of cut, b_{dj}^i is the edge length of the trapezoid, r is the nose radius and k_j^i is the angle that defines the orientation of an element edge for each section.

3.2 Stability Limit Solution

It is shown that the stability model in boring operations reduces to a 1D eigenvalue problem by the help of a reduced transfer function matrix and solved analytically even including the insert nose radius effect [51].

The dynamic chip thickness is calculated and its relation with dynamic forces is provided in Eq. 3.8:

$$\begin{Bmatrix} F_{y_j}^i \\ F_{z_j}^i \end{Bmatrix} = b_j^i [A_j^i] \begin{Bmatrix} \Delta Y \\ \Delta Z \end{Bmatrix} \quad 3.8$$

where:

$$\begin{cases} [A_j^i] = \begin{bmatrix} A_{j11}^i & A_{j12}^i \\ A_{j21}^i & A_{j22}^i \end{bmatrix} = \begin{bmatrix} \sin k_j^i & \cos k_j^i \\ \cos k_j^i & -\sin k_j^i \end{bmatrix} \begin{bmatrix} K_{nc} \\ K_{fc} \end{bmatrix} \begin{bmatrix} -\tan k_j^i & -1 \end{bmatrix} & i = 1 \\ [A_j^i] = \begin{bmatrix} A_{j11}^i & A_{j12}^i \\ A_{j21}^i & A_{j22}^i \end{bmatrix} = \begin{bmatrix} -\sin k_j^i & \cos k_j^i \\ \cos k_j^i & \sin k_j^i \end{bmatrix} \begin{bmatrix} K_{nc} \\ K_{fc} \end{bmatrix} \begin{bmatrix} -\tan k_j^i & 1 \end{bmatrix} & i = 2,3 \end{cases} \quad 3.9$$

We know that $[A_j^i]$ and $\begin{Bmatrix} \Delta Y \\ \Delta Z \end{Bmatrix}$ represent the directional coefficient matrix and total dynamic displacements in y and z directions.

$$\begin{Bmatrix} \Delta Y \\ \Delta Z \end{Bmatrix} = (1 - e^{-i\omega_c \tau}) [G(i\omega_c)] \left[\begin{Bmatrix} F_{y_1} \\ F_{z_1} \end{Bmatrix} + \begin{Bmatrix} F_{y_2} \\ F_{z_2} \end{Bmatrix} + \dots + \begin{Bmatrix} F_{y_m} \\ F_{z_m} \end{Bmatrix} \right] \quad 3.10$$

$$[G(i\omega_c)] = [G_c(i\omega_c)] + [G_w(i\omega_c)] = \begin{bmatrix} \phi_{yy} & 0 \\ 0 & 0 \end{bmatrix} \quad 3.11$$

where m stands for the total number of chip area elements and the assumption is that the transfer function matrix $[G(i\omega_c)]$ only contains the transfer function in the y direction because, in almost all boring operations, the tool and the workpiece are much more rigid in the z (feed) direction and can be ignored. Consequently, the following is the transfer function matrix:

$$[F_j] e^{i\omega_c t} = b_j^i (1 - e^{-i\omega_c \tau}) [A_j] [G(i\omega_c)] \sum_{j=1}^m [F_j] e^{i\omega_c t} \quad 3.12$$

if and only if its determinant is zero, Eq. 3.12 has a non-trivial solution, which results in:

$$\det[[I] + \Lambda [G_0(i\omega_c)]] = 0 \quad 3.13$$

$$[G_0(i\omega_c)] = [A_j] [G(i\omega_c)] \quad 3.14$$

$$\Lambda = b_j (1 - e^{-i\omega_c \tau}) \quad 3.15$$

The stability limit can be computed using Eq. 3.16 because the stability model has been simplified to an eigenvalue problem.

$$b_{j_{lim}} = -\frac{1}{2} \Lambda_R (1 + \lambda^2) \quad 3.16$$

where:

$$\lambda = \frac{\Lambda_I}{\Lambda_R} = \frac{\sin \omega_c \tau}{1 - \cos \omega_c \tau} \quad 3.17$$

One can deduce that the $b_{j_{lim}}$ is the elemental stable depth of cut and the total stable depth of cut can be obtained by multiplying it with the total numbers of elements.

3.3 Solution Procedure

In the first step, the dynamic chip thickness in the machine tool coordinates is formulated. Then, the elemental depth of cut is obtained by dividing the nose radius value into small

elements, and this elemental depth of cut is assumed to be equal for all sections. The elemental approach angle is calculated using the length of each trapezoid, as shown in Eq. 3.6.

Equation 3.8 demonstrates the relation of elemental forces and dynamic chip thickness. By summing all the elemental forces along the chip area and multiplying them with the transfer function matrix, the total dynamic displacement can be calculated. Then, using Eq. 3.12, the problem is transformed into an eigenvalue problem. By solving the eigenvalue problem, the elemental stable depth of cut is calculated. The total stable depth of cut is obtained by multiplying the elemental depth of cut by the total number of elements.

3.4 Experimental Analysis of Miniature Boring Tools Dynamics

In this project, the main objective is to enhance the design of a miniature boring tool. This will be achieved through process modeling and attempts to modify the geometrical properties of the tool's cutting edge, ultimately reducing the forces, especially radial force. Therefore, measuring the forces during the cutting process is of utmost importance for experimental validation of the force model.

Due to the cylindrical shape of the tool and tool holder, a fixture is necessary to clamp them on the dynamometer, resulting in a flexible tool-holder-fixture-dynamometer configuration. Moreover, the physics of the boring process itself makes it susceptible to vibrations, necessitating a dynamic analysis of the boring process.

Two tool holders, varying in terms of tolerance and length, were produced by the tool manufacturer, and sent for experimentation. Additionally, two sets of tools with different lengths were also provided (refer to Table 3.1). Consequently, four different configurations (see Figure 3.3) for the tool-holder were investigated by two experimental setups which were prepared to measure the stiffness and modal analysis of the structures.

Table 3.1. Tool and tool holder's length and tolerance.

Component	Length (mm)	Tolerance
Tool holder1 (long)	100	Loose
Tool holder2 (short)	57	Tight
Tool1 (long)	25	-
Tool2 (short)	15	-

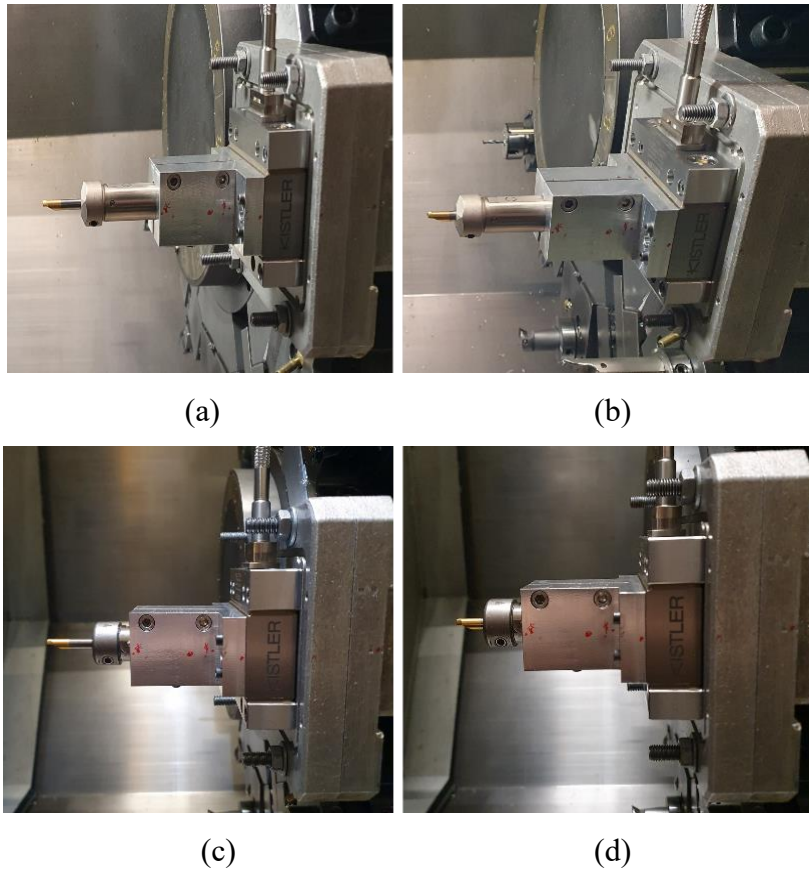
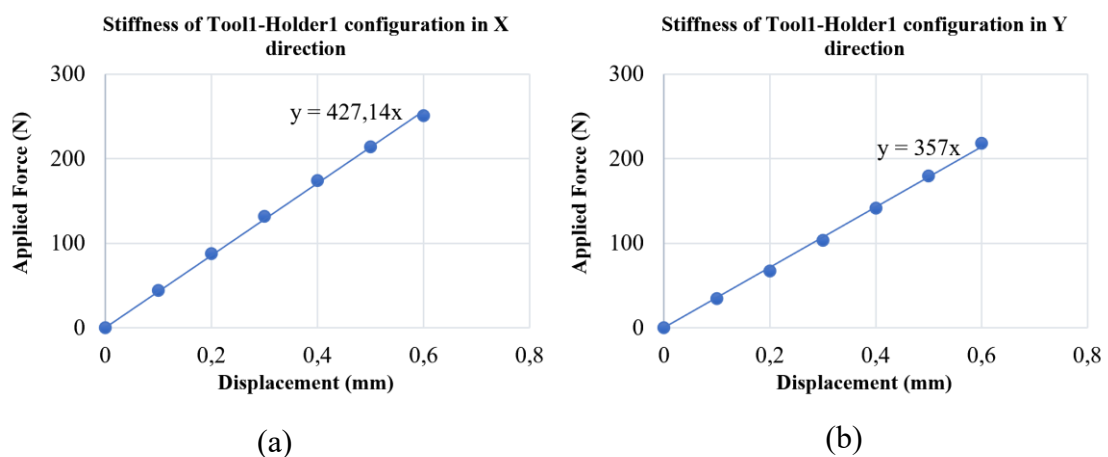
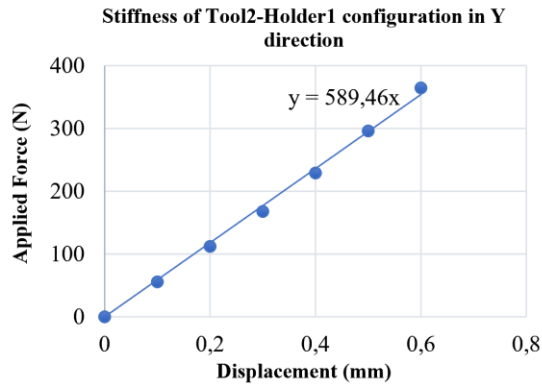


Figure 3.3. four tool-holder configurations a) tool1-holder1 b) tool2-holder1 c) tool1-holder2 d) tool2-holder2

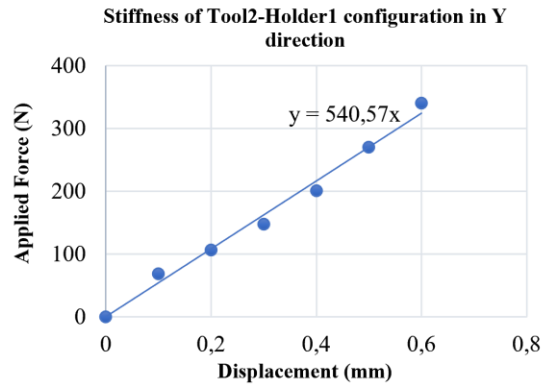
3.4.1 Stiffness Measurement of Miniature Boring Tools for Different Tool-Holder Configurations

An experimental setup has been prepared to measure the stiffness of the tool for different configurations (see Figure 3.3). By exerting a constant value of displacement on the tip point of the tool and measuring the applied force, the stiffness graph of the tool is obtained. Stiffness graphs for four different tool-holder configurations can be seen in Figure 3.4 and Figure 3.5.



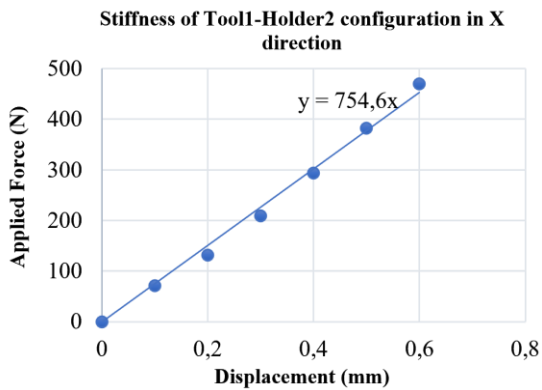


(c)

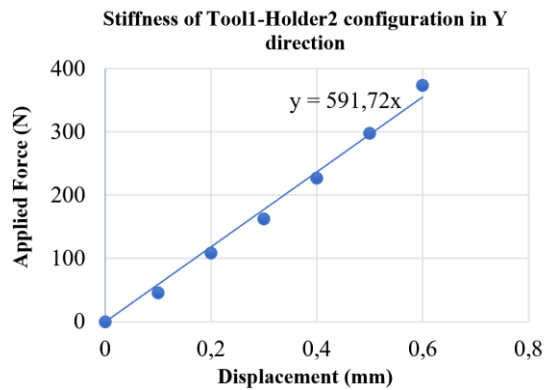


(d)

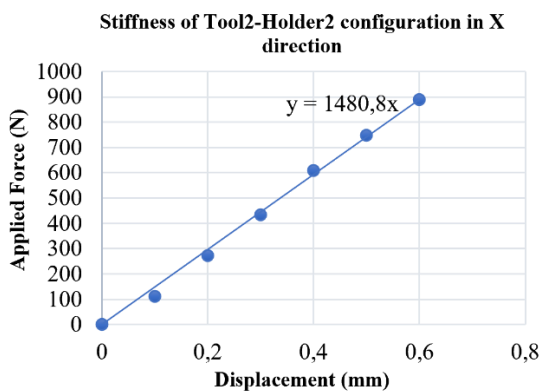
Figure 3.4. Force-displacement curve used to compute stiffness of tool using tool holder1 (tool holder with loose tolerance).



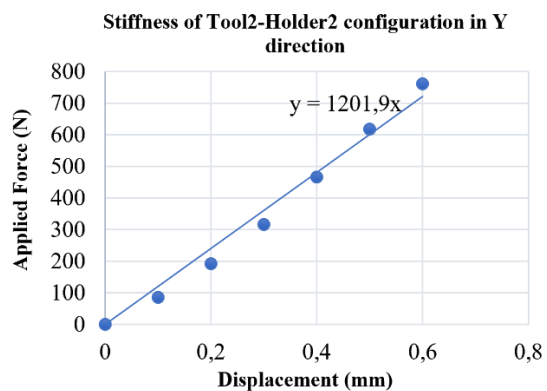
(a)



(b)



(c)



(d)

Figure 3.5. Force-displacement curve used to compute stiffness of tool using tool holder2 (tool holder with tight tolerance).

The stiffness of the tool can be calculated using the force-displacement curve which is obtained from experiments. Tool's stiffness can be calculated using Eq. 3.18 as follow:

$$\mathcal{U} = \frac{\Delta F}{\Delta v} \quad 3.18$$

where \mathcal{U} , ΔF , and Δv represent the stiffness, force, and displacement difference respectively. The stiffness values are calculated for each tool-holder configuration in x and y directions. Results showed that the tool is more rigid in the x direction. The reason for this rigidity is the shape of the tool at its tip point (see Figure 3.6). One can deduce that the cylindrical shape of the tool is cut in the y direction, which makes it more flexible in the y direction than in the x direction.

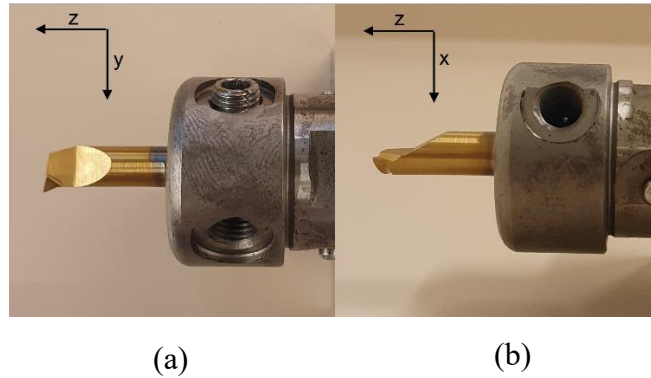


Figure 3.6. a) top and b) side view of a miniature boring tool.

Additionally, a holder with tight tolerances and shorter length results in higher rigidity for both long and short tools. With tighter tolerances, the holder firmly secures the tool, leading to higher clamping stiffness. Furthermore, if we consider the structure as a cantilever beam, a shorter length contributes to higher stiffness. As mentioned, a shorter length of the tool leads to increased rigidity. Consequently, the shorter tool (Tool2) clamped by the shorter holder (Holder2) exhibits higher stiffness and rigidity.

3.4.1 Modal Analysis of Miniature Boring Tools for Different Holder-Tool Configurations

Modal test setup was prepared to investigate the dynamics of miniature tools for different tool-holder configurations (see Figure 3.7). The modal test setup consists of an impact hammer, an accelerometer, and a data acquisition system. The objective is to measure the tool tip's FRF and utilize the modal values in the developed chatter stability model. The data is collected and analyzed by CutPro [52].

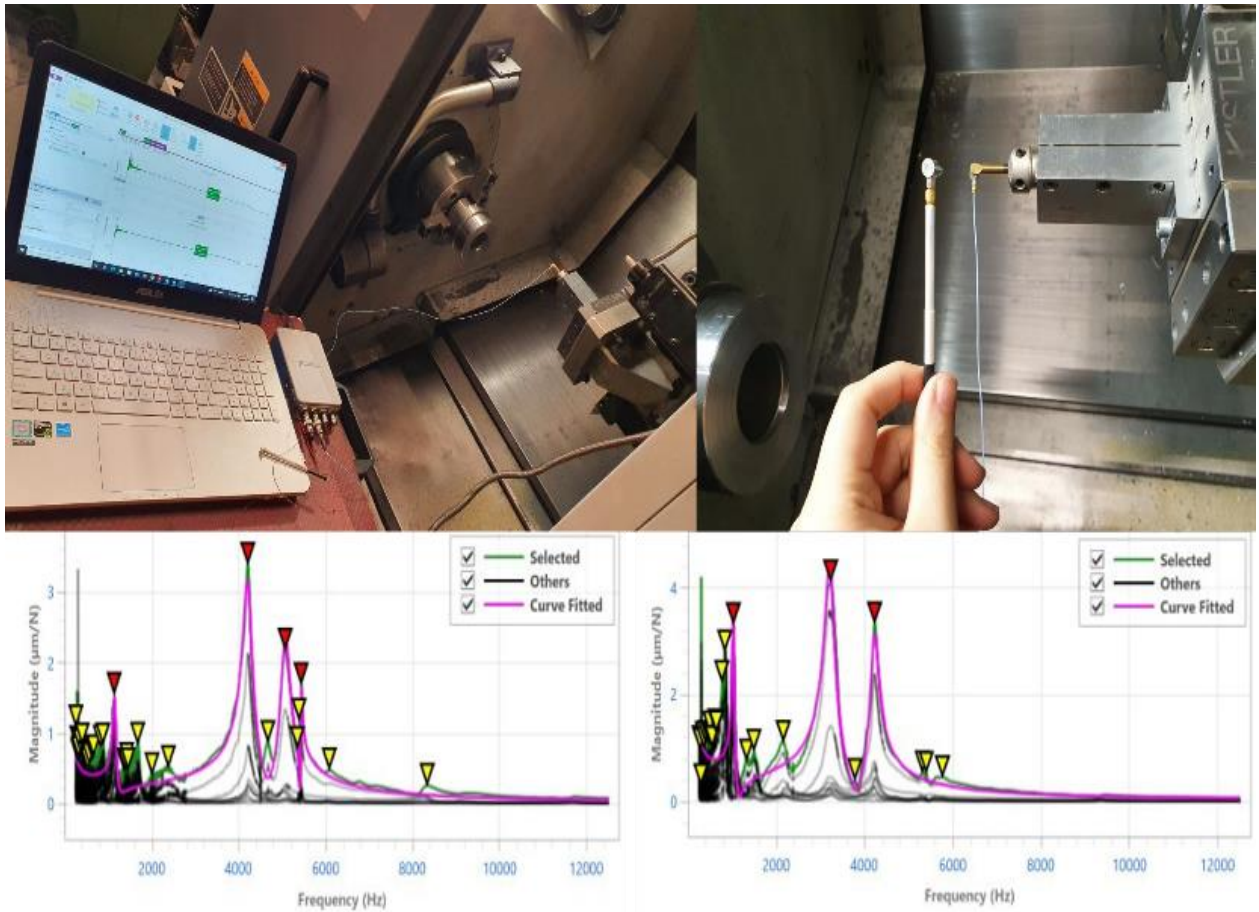
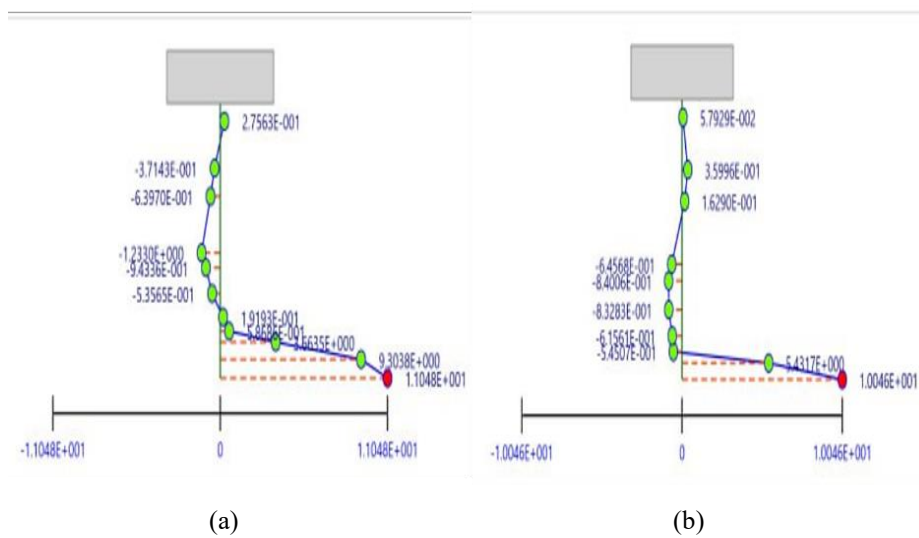


Figure 3.7. Modal test setup and examples of measured FRFs' graphs.

As can be seen in Figure 3.7 the tool tip FRF was measured in y direction for four different configurations. Mode shapes for tool-holder configurations are provided in Figure 3.8.



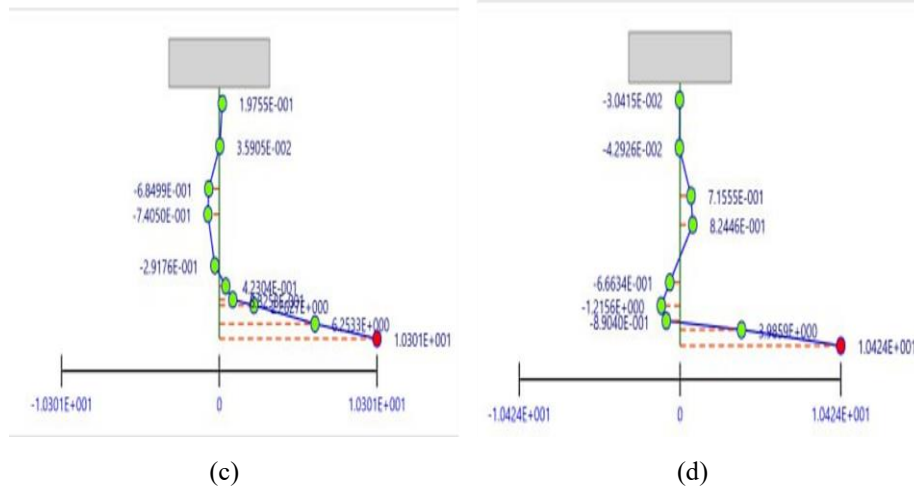


Figure 3.8. Mode shapes for a) Tool1-holder1 b) Tool2-holder1 c) Tool1-holder2 d) Tool2-holder2 configurations

By further investigation one can deduce that these mode shapes (see Figure 3.8) are related to the tool which are the most flexible component of each configuration.

Table 3.2. Modal stiffness of different Tool-Holder configurations measured by modal tests.

Tool-Holder configuration	Modal stiffness (N/m)
Tool1_Holder1	3.35×10^6
Tool2_Holder1	9.72×10^6
Tool1_Holder2	1.08×10^7
Tool2_Holder2	3.62×10^7

In addition, by comparing their stiffness values measured through modal tests (refer to Table 3.2), it becomes evident that the Tool2-Holder2 configuration is the most rigid structure.

3.5 Model Verification

Two strategies are taken into consideration in order to validate the modified model. The first strategy is to use data from the literature to validate the model. The second approach involves conducting chatter tests during the hole enlarging process using miniature boring tools, and experimental data is used to validate the model.

3.5.1 Model Verification from Literature

As mentioned earlier, the proposed model in Section 3.1 is adapted from [51] stability model. The analytical model is used to develop a simulation code for predicting the

stable depth of cut. The parameters used in [51] (refer to Table 3.3) are employed to verify the proposed model in this study.

Table 3.3. Parameters used in the verification of boring chatter experiments in [51].

Approach angle (degree)	Cutting force coefficient, K_f (Mpa)	Natural frequency of the tool (Hz)	Stiffness of the tool (N/m)	Damping ratio
0	700	3690	2.3×10^7	0.012

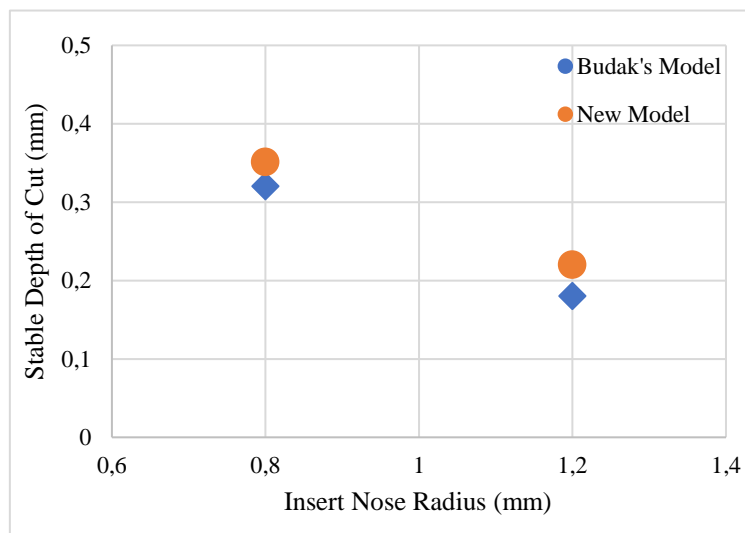


Figure 3.9. Comparison of the predicted stable depth of cut by Budak's and adapted model.

As can be seen from Figure 3.9 the newly developed stability model's simulation results are in good agreement with previously predicted and experimentally verified values.

3.5.2 Model Verification with Experiments

In order to acquire the dynamic system's absolute stability limit experimentally during hole enlarging operation, chatter experiments were carried out.

Due to the lower spindle speeds and single cutting tooth used in boring operations, the stability lobes are much narrower than those used in milling operations. The depths of cut used in the chatter experiments were chosen to confirm the stable and unstable cutting zones. The experiments therefore aim to confirm the predicted absolute stability limits.

Experiments were done on the MORI SEIKI NL1500 lathe machine. In experiments miniature boring tools with 14° rake 6° oblique angles and a rigid workpiece were used. Also, A feed rate of 0.03 mm/rev was used for all tests.

The most important part of these experiments is that they were conducted for four configurations of the tool-holder. Figure 3.10 shows the experimental and predicted stable depth of cut for each of the tool-holder configurations.

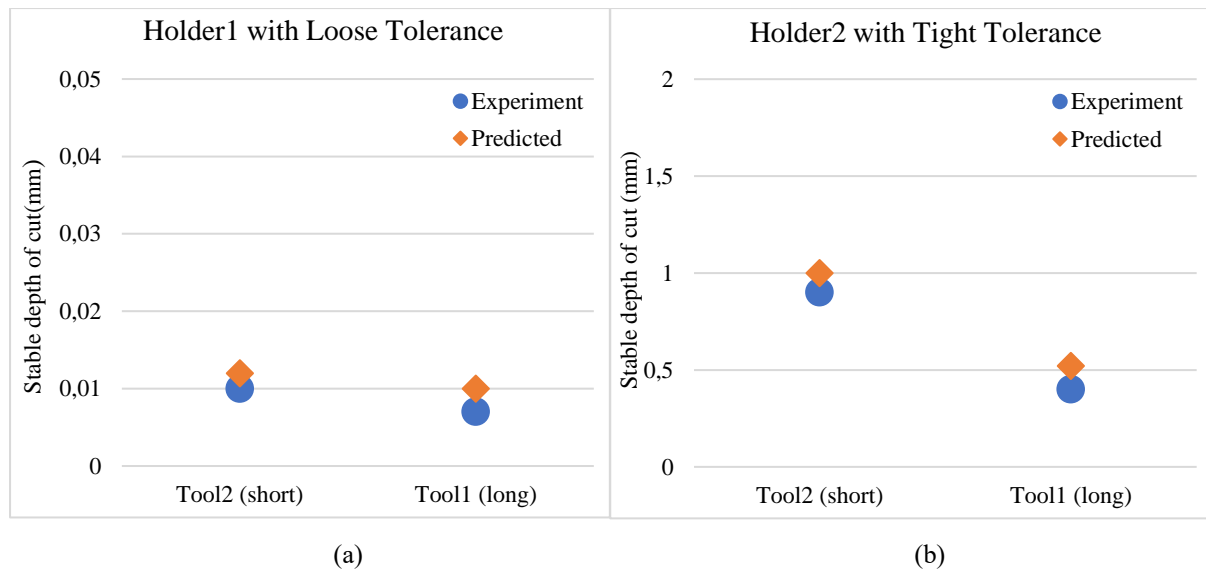


Figure 3.10. Chatter test and simulation results for stable depth of cut using tool1 and tool2 clamping with a) Holder1 b) Holder2.

The predicted values and experimental results are in good agreement, allowing us to obtain the stable depth of cut for miniature boring tools with positive approach angles. As can be seen, the stable depth of cut is higher for both tool holders when clamping a shorter tool. Additionally, the stable depth of cut is significantly higher when using a holder with tight tolerance for both tools (Tool1 and Tool2), which is a result of its clamping rigidity.

4. Design Improvement of Miniature Boring Tools

4.1 Simulation Results

For the calculation of cutting forces, an analytical force model has been developed based on different chip geometries resulting from various engagements between the tool and workpiece. Cutting tests, as mentioned in Section 2.7, were conducted to validate the force model, and the results showed good agreement. Therefore, we can utilize the force model in simulations to extract forces under different cutting conditions and explore various geometrical properties for optimizing the tool edge geometry.

The geometrical properties of the cutting tool edge, depth of cut, and feed rate play a significant role in chip shape generation, making it more complex to calculate the chip area for certain configurations (see Figure 2.5). To investigate the effects of different parameters, simulations have been performed, and the results are presented in the graphs below.

4.1.1 Effect of Nose Radius and Approach Angle on the Forces

To examine the impact of approach angle and nose radius on the forces, the depth of cut plays a crucial role in determining their respective engagement proportions. Consequently, three different depths of cut have been selected, and their effect on approach angle and nose radius has been investigated under the desired cutting conditions, as outlined in Table 4.1. For this study, 1050 steel has been chosen as the workpiece material, and the cutting conditions have been carefully selected based on the requirements specified by the tool manufacturer (refer to Table 4.2).

Table 4.1. Depth of cut, nose radius and approach angle values used for simulations.

Depth of Cut (mm)	Nose Radius (mm)	Approach angle (degree)
0.05	0.1, 0.15, 0.2, 0.25, 0.3	-10, -5, 0, 5, 10
0.15	0.1, 0.15, 0.2, 0.25, 0.3	-10, -5, 0, 5, 10
0.25	0.1, 0.15, 0.2, 0.25, 0.3	-10, -5, 0, 5, 10

Table 4.2. Cutting tests' conditions used for simulations.

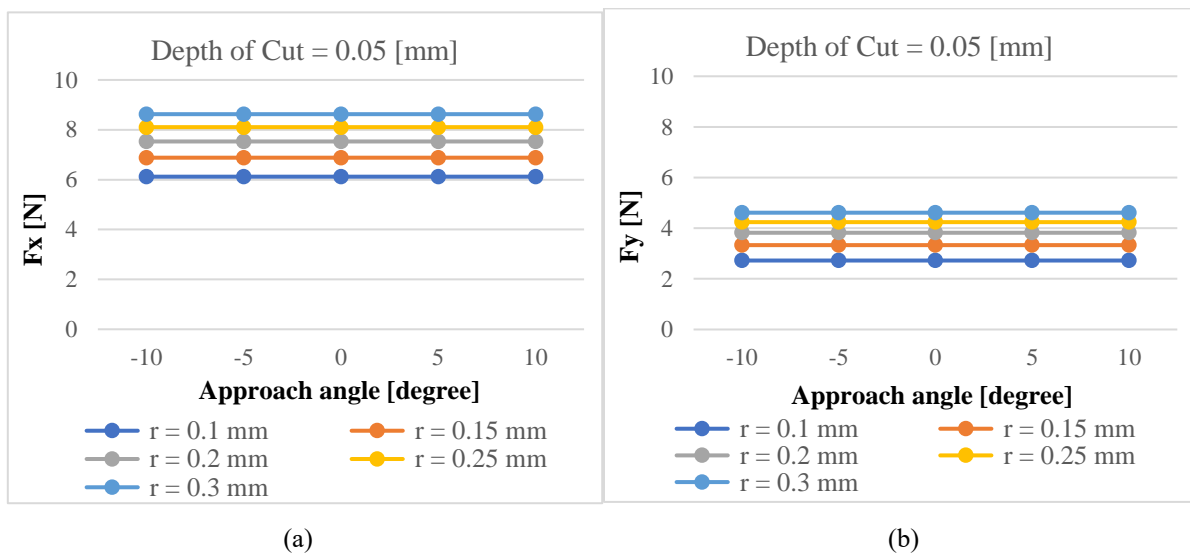
Material	Cutting Speed (m/min)	Feed Rate (mm/rev)
1050 Steel	110	0.03

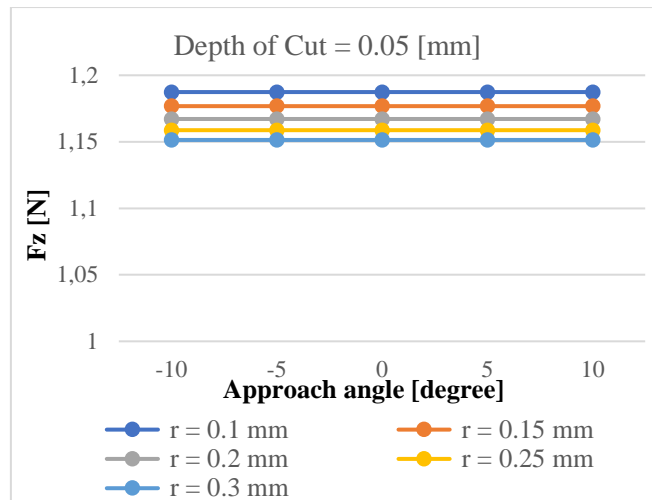
Case 1: 0.05 mm Depth of Cut

As depicted in the graphs below (Figure 4.1), it is evident that the depth of cut is smaller than all the selected tool nose radii. Consequently, the part of the tool edge with the approach angle does not engage with the workpiece. Therefore, altering the approach angle in this case has no impact on the cutting forces.

Furthermore, it is observed that the tool with the largest nose radius exhibits the highest cutting forces due to its larger chip area, while the tool with the smallest nose radius results in the lowest cutting forces.

Additionally, it can be observed that the forces in the radial direction surpass those in the feed direction. This phenomenon is demonstrated in Figure 2.7, where the directions of radial and feed forces continuously change along the nose radius. The compensation of forces in the feed direction ultimately results in the dominance of the radial force.





(c)

Figure 4.1. Acquired forces a) in x direction, b) in y (radial) direction, and c) in z (feed) direction from simulations using various nose radius and different approach angles for 0.05 mm depth of cut.

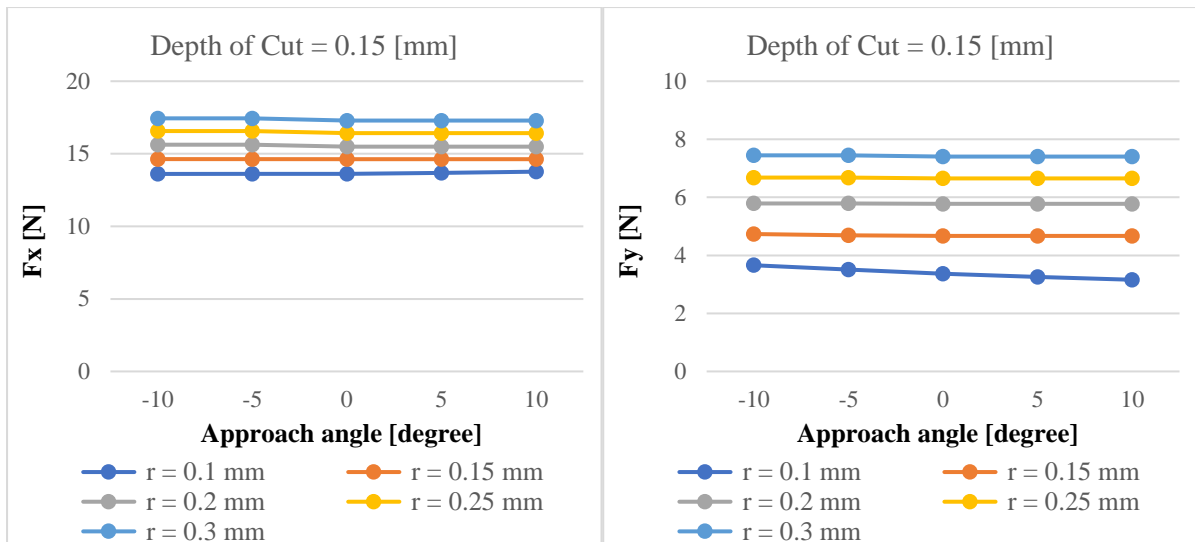
Case 2: 0.15 mm Depth of Cut

In this case, the approach angle does not significantly impact the direction of the tangential force. However, it does lead to minor variations in the chip area, which in turn cause small changes in the tangential forces.

When the approach angle is negative, the radial forces compensate each other. However, this results in an increase in the feed force, as they now act in the same direction and contribute to a higher total feed force.

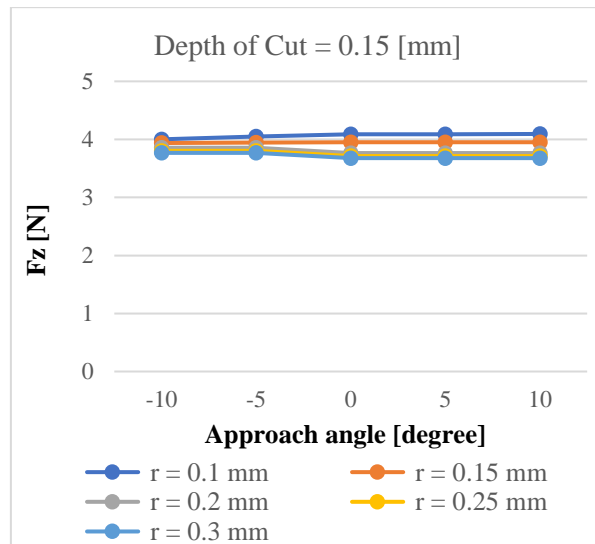
Changing the approach angle from -10 to 10 reduces the forces in the radial direction due to compensation. However, as mentioned earlier, when the depth of cut is small, the engagement proportion becomes the determining factor for the effect of the approach angle. While the approach angle does not significantly impact the force magnitude, a slight change can be observed in cases where the nose radius exceeds 0.1 mm, specifically in the -10 and -5 approach angles. This can be attributed to geometric factors. In these two cases, the chip area includes a very small section of the approach angle, which influences the forces. As the area is extremely small, the calculated approach angle in the analytical model remains the same for both cases, resulting in a similar effect on the forces.

Similar conclusions can be drawn for the feed force. However, in contrast to the radial forces, the feed forces will increase when the approach angle changes from -10 to 10.



(a)

(b)



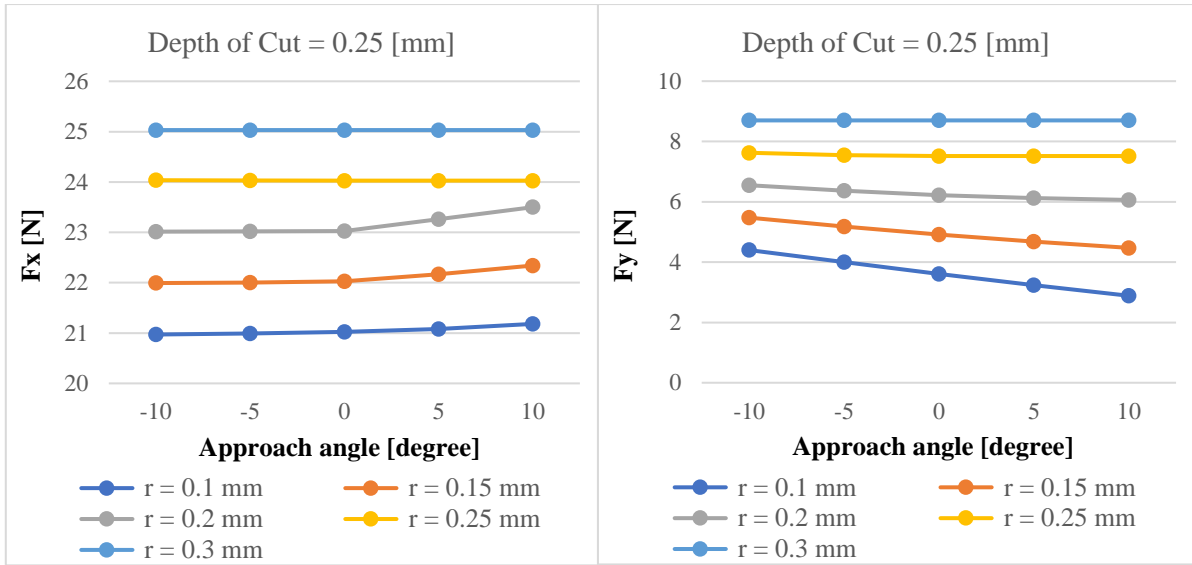
(c)

Figure 4.2. Acquired forces a) in x direction, b) in y (radial) direction, and c) in z (feed) direction from simulations using various nose radius and different approach angles for 0.15 mm depth of cut.

Case 3: 0.25 mm Depth of Cut

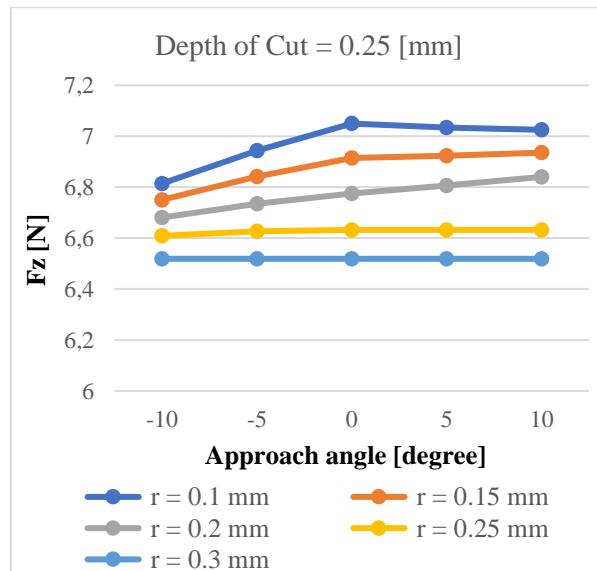
Similar to the previous case, the tangential force remains unaffected by the change in approach angle. However, minor changes can be observed due to variations in the chip area resulting from the adjustment of the approach angle.

In this particular case, where the depth of cut exceeds the values of most nose radii, the influence of the approach angle on the cutting forces becomes apparent. When the approach angle is changed from -10 to 10, the radial forces compensate each other due to their direction along the cutting edge. As a result, the radial forces decrease, while the feed forces increase.



(a)

(b)



(c)

Figure 4.3. Acquired forces a) in x direction, b) in y (radial) direction, and c) in z (feed) direction from simulations using various nose radius and different approach angles for 0.25 mm depth of cut.

4.1.2 Effect of Oblique and Rake Angle on the Forces

To investigate the effects of the rake and oblique angles on the forces, two depths of cut (0.12 and 0.25 mm) have been chosen. For each depth of cut, all other parameters remain constant while the oblique and rake angles vary within the specified limits. The workpiece material selected for the study is 1050 steel, and a cutting tool with a 0.2 mm nose radius and an 8-degree approach angle has been utilized.

The geometrical properties of the cutting tool edge and the specific cutting conditions employed for simulations are detailed in Table 4.3 and Table 4.4, respectively.

Table 4.3. Depth of cut, oblique and rake angle values used for simulations.

Depth of Cut (mm)	Oblique angle (degree)	Rake angle (degree)
0.12	0, 2, 6, 12, 16, 20	0, 5, 10, 14, 20, 25, 30
0.25	0, 2, 6, 12, 16, 20	0, 5, 10, 14, 20, 25, 30

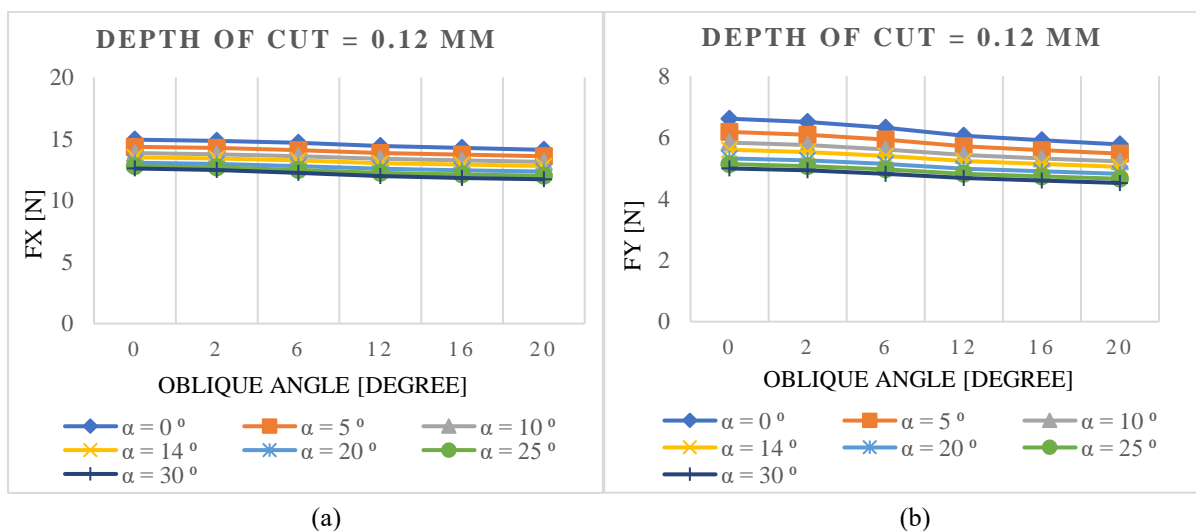
Table 4.4. Cutting tests' conditions used for simulations.

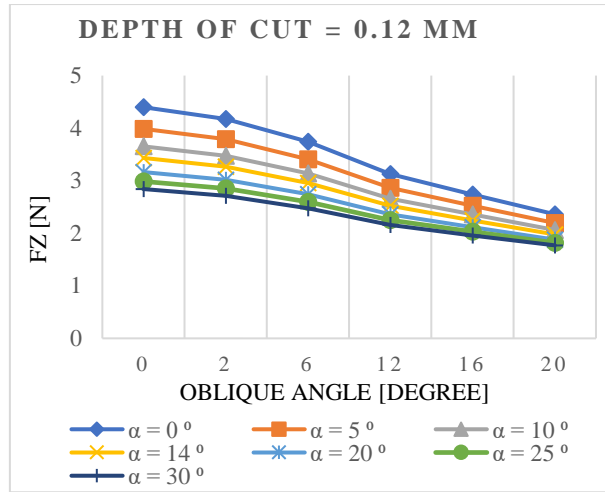
Material	Cutting Speed (m/min)	Feed Rate (mm/rev)
1050 Steel	110	0.03

Increase in the rake angle leads to a decrease in forces in all directions, primarily due to the reduced resistance of the rake face during chip collision with it.

Generally, an increase in the oblique angle is expected to cause an increase in the radial force and a decrease in the feed force. However, in cases where the depth of cut is smaller than the nose radius, the engagement of the tool's nose with the workpiece occurs near the top of the nose. As a result, the rake angle becomes dominant in this region. Since an increase in the rake angle reduces the forces, the variation of rake and oblique angles in this specific engagement area contributes to force reduction.

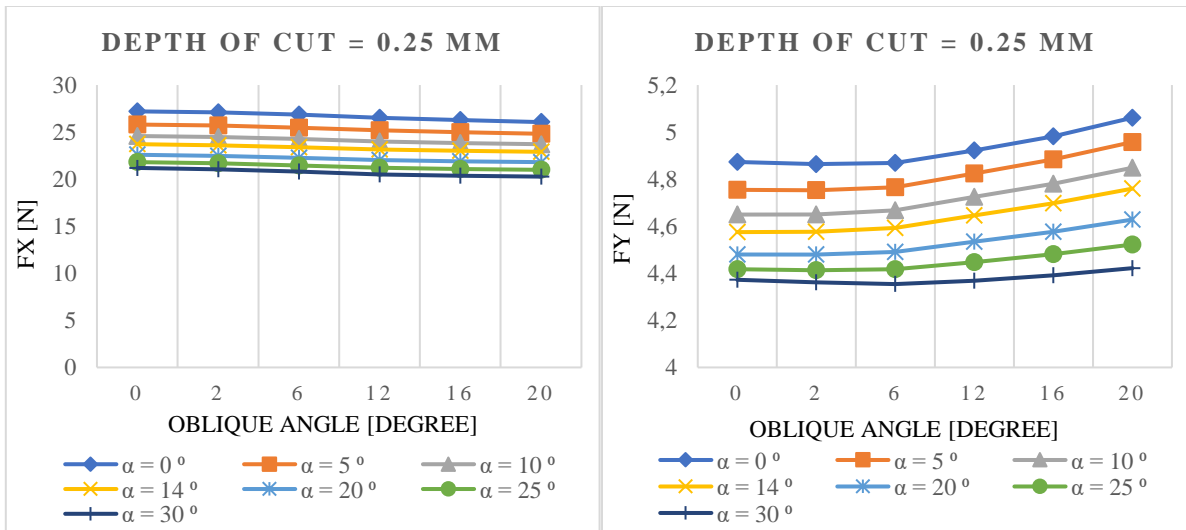
Conversely, when the depth of cut exceeds the nose radius and both the nose and the straight cutting edge of the tool engage with the workpiece, the effects of oblique and rake angles become more pronounced. The radial force increases while the feed force decreases with an increase in the oblique angle.





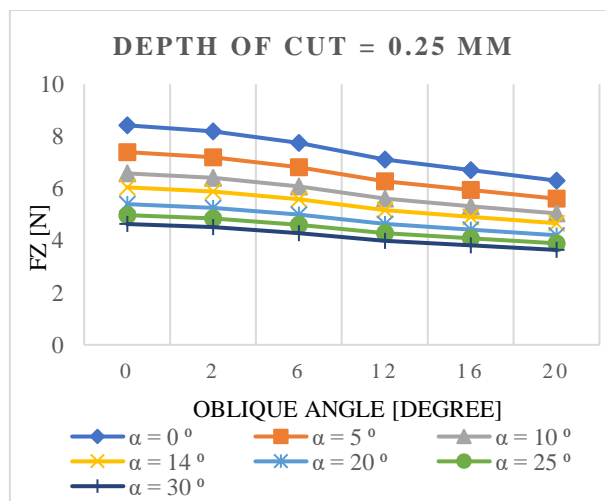
(c)

Figure 4.4. Acquired forces a) in x direction, b) in y (radial) direction, and c) in z (feed) direction from simulations using various oblique and rake angles for 0.12 mm depth of cut.



(a)

(b)



(c)

Figure 4.5. Acquired forces a) in x direction, b) in y (radial) direction, and c) in z (feed) direction from simulations using various oblique and rake angles for 0.25 mm depth of cut.

In another scenario, the effect of the rake angle has been investigated when it does not impact the orthogonal data but solely affects the geometrical properties of the tool edge. All parameters remain the same as before, except for the rake angle, which has been changed from 14 to 20 degrees (refer to Figure 4.6 and Figure 4.7).

As observed from graphs below, in both cases where the depth of cut is higher or smaller than the nose radius, when the rake angle solely impacts the geometric properties of tool edge without affecting the orthogonal data (shear angle, friction angle, and shear stress), the reduction in forces is less pronounced compared to situations where the rake angle influences both the orthogonal data and geometric parameters. However, this phenomenon is not evident in the radial and feed forces. Therefore, we can conclude that the effect of geometric properties on these two forces is more dominant than the effect of orthogonal data.

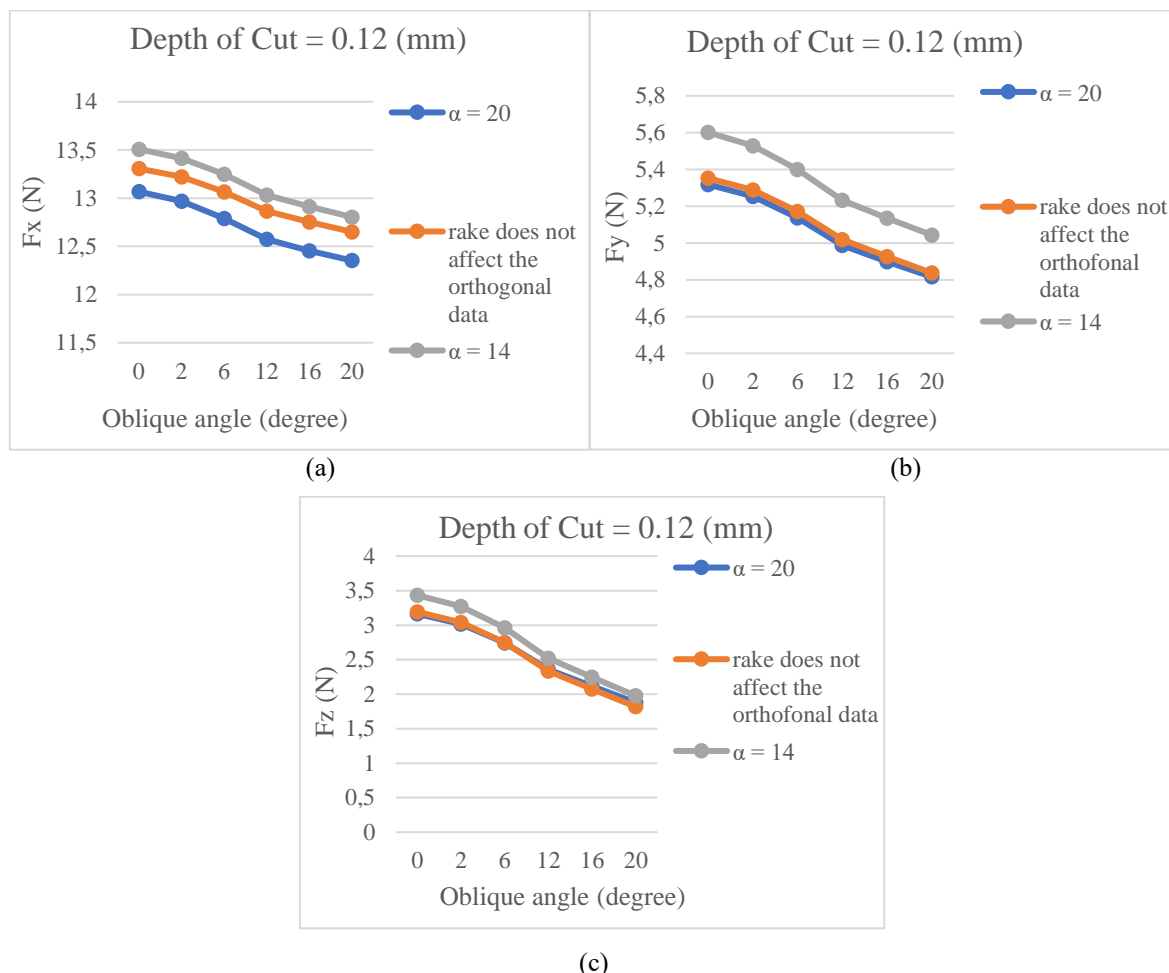


Figure 4.6. Acquired forces a) in x direction, b) in y (radial) direction, and c) in z (feed) direction from simulations using 14 and 20 degrees of rake angles affecting and without affecting orthogonal data for 0.12 mm depth of cut.

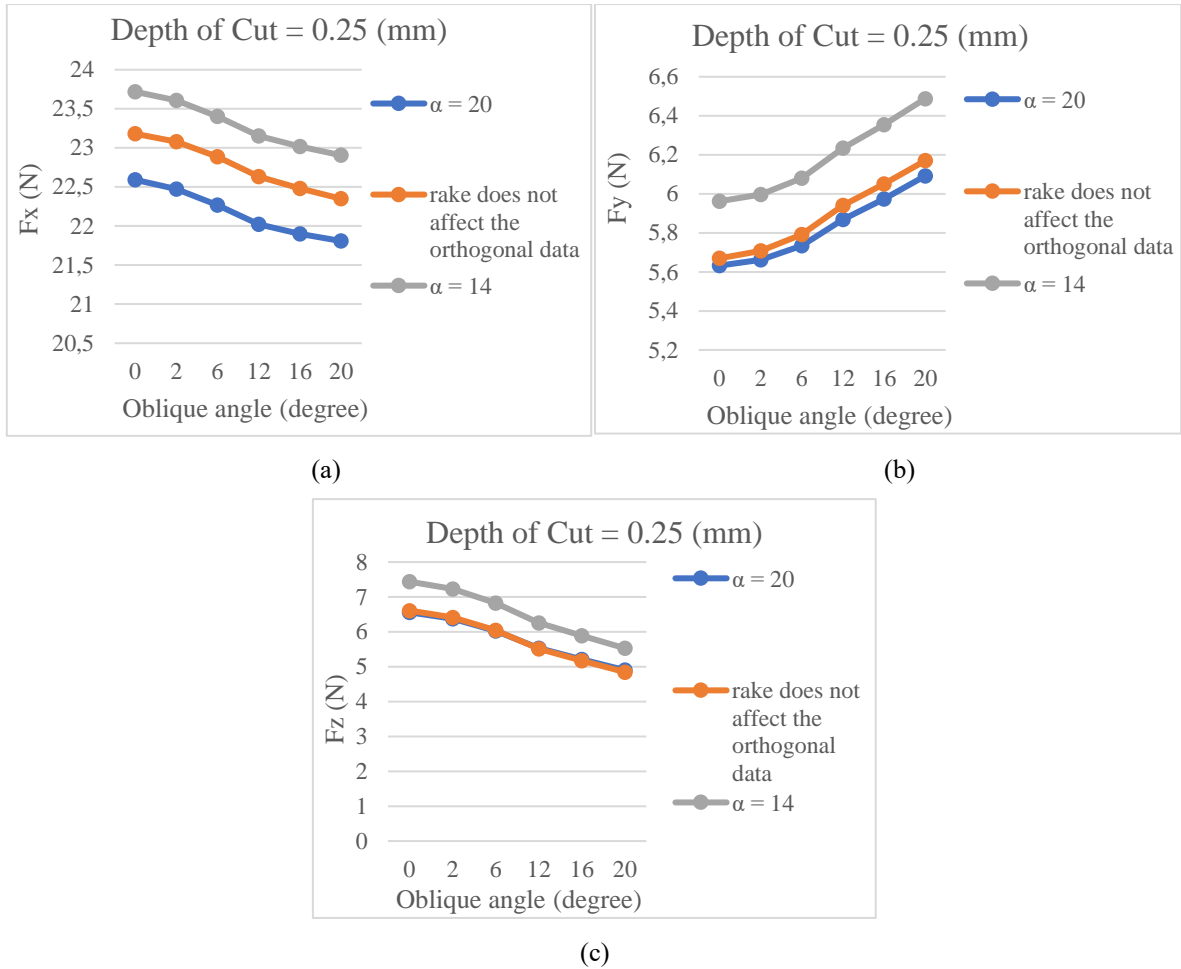
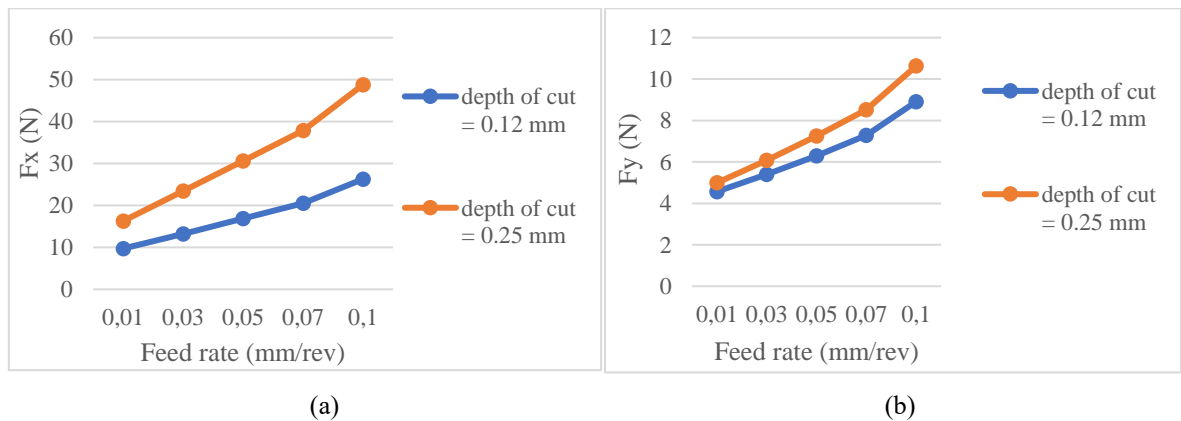
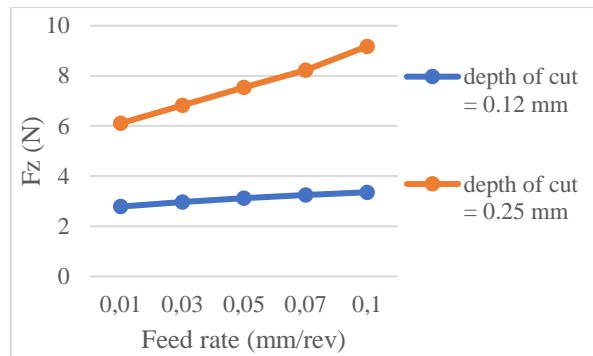


Figure 4.7. Acquired forces a) in x direction, b) in y (radial) direction, and c) in z (feed) direction from simulations using 14 and 20 degrees of rake angles affecting and without affecting orthogonal data for 0.25 mm depth of cut.

4.1.3 Effect of Feed Rate

Increasing the feed rate leads to an increase in forces for both high and small depths of cut, primarily due to the enlarged chip area, as illustrated in the graphs below. Additionally, higher feed rate values result in scallop marks on the workpiece, which is undesirable in precision machining processes.





(c)

Figure 4.8. Acquired forces a) in x direction, b) in y (radial) direction, and c) in z (feed) direction from simulations using various feed rates for 0.12 mm and 0.25 mm depths of cut.

4.1.4 Discussion on Simulation Results

The results obtained from simulations conducted under various cutting conditions using different tool edge geometric parameters reveal the following findings:

- Higher values of feed rate and nose radius lead to increased cutting forces.
- When the depth of cut is smaller than the nose radius, the approach angle has no effect on the forces. However, when the depth of cut exceeds the nose radius, higher approach angles result in lower radial forces.
- Although the combination of rake and oblique angles leads to reduced forces in all directions when the depth of cut is smaller than the nose radius, when the depth of cut exceeds the nose radius, higher oblique angles increase the radial forces.

In conclusion, the aim of these simulations is to provide optimal parameters for tool edge geometric properties to achieve more precise bored holes. Based on the simulation results, manufacturers' requirements, and ease of production, certain geometric parameters have been suggested to the manufacturer. In addition, miniature boring tools are employed for hole enlargement, mostly with a maximum diameter of 6 or 8 mm and a small cutting edge.

It has been demonstrated that smaller tool radii result in smaller forces, but the strength of the tool nose is also reduced. Therefore, a nose radius of 0.1-0.3 mm has been recommended as a compromise between the two factors. When the depth of cut exceeds the nose radius, higher approach angles decrease radial forces, but excessively high values can weaken the tool tip. Hence, an approach angle of 8-15 degrees has been suggested for cases where high depth of cut is desired. Rake angle has a greater impact on forces compared to oblique angle and is dominant when the depth of cut is smaller. Additionally, when the depth of cut exceeds the nose radius, higher oblique angles increase radial forces. Therefore, oblique angles of 6-15 degrees, for easy chip removal, and rake angles of 10-20 degrees have been recommended.

Furthermore, the model does not investigate the effect of clearance angle, back approach angle, and hone radius. However, it is necessary to have a clearance angle and back approach angle to reduce friction between the new workpiece surface and the tool. It should be noted that excessively high values of both parameters can weaken the tool tip. Additionally, due to the small values of the feed rate, the back approach angle does not significantly affect the forces. Moreover, hone radius enhances the strength of the cutting edge, improves the quality of the cut surface, and has a positive impact on vibrations. However, it also increases the cutting forces and influences the minimum chip thickness that can be removed. Taking all these factors into consideration, along with considerations of production feasibility, the tool manufacturer has produced 5 different tools with varying geometric properties. Experiments have been conducted using these tools, and the results will be further investigated in the subsequent section.

4.2 Experimental Results

Cutting tests were conducted using sharp tools to investigate the effect of tool edge geometrical properties on the cutting forces, surface roughness, cylindricity, and circularity of the workpiece. Tests were performed under the desired cutting conditions as presented in Table 4.5.

The chosen workpiece material for the study was 1050 Steel. Five tools with different tool edge geometrical properties were selected (see Table 4.6). The first tool in Table 4.6 was selected as the reference tool, and the geometric parameters of the other tools were adjusted based on it. Each tool had only one parameter that differed from the reference tool, allowing for the examination of the specific parameter's impact on the cutting forces, surface roughness, cylindricity, and circularity of the workpiece.

Table 4.5. Cutting test conditions for experiments

Workpiece material	Cooling condition	Cutting speed (m/min)	Feed rate (mm/rev)	Depth of cut (mm)
AISI 1050 Steel	Dry machining	110	0.03	0.12

Table 4.6. Geometrical and material properties of miniature boring tools

Tool code	Material	Coating	Rake angle (degree)	Oblique angle (degree)	Clearance angle (degree)	Approach angle (degree)	Nose radius (mm)	Honing time (min)
T-038	TC402	TiN	14	6	10	8	0.2	3
T-042	TC402	TiN	14	6	10	8	0.2	6
T-043	TC402	TiN	14	12	10	8	0.2	3
T-046	TC402	TiN	20	6	10	8	0.2	3
T-047	TC402	TiN	14	6	10	12	0.2	3

To measure the cutting forces using a dynamometer during the boring process, a fixture was required to clamp the tool holder onto the dynamometer, as depicted in Figure 4.9 (a).

Given that these miniature boring tools were primarily used for precision hole enlarging processes, the depth of cut selected was generally small. Similarly, to achieve low levels of surface roughness, the feed rate was set to small values.

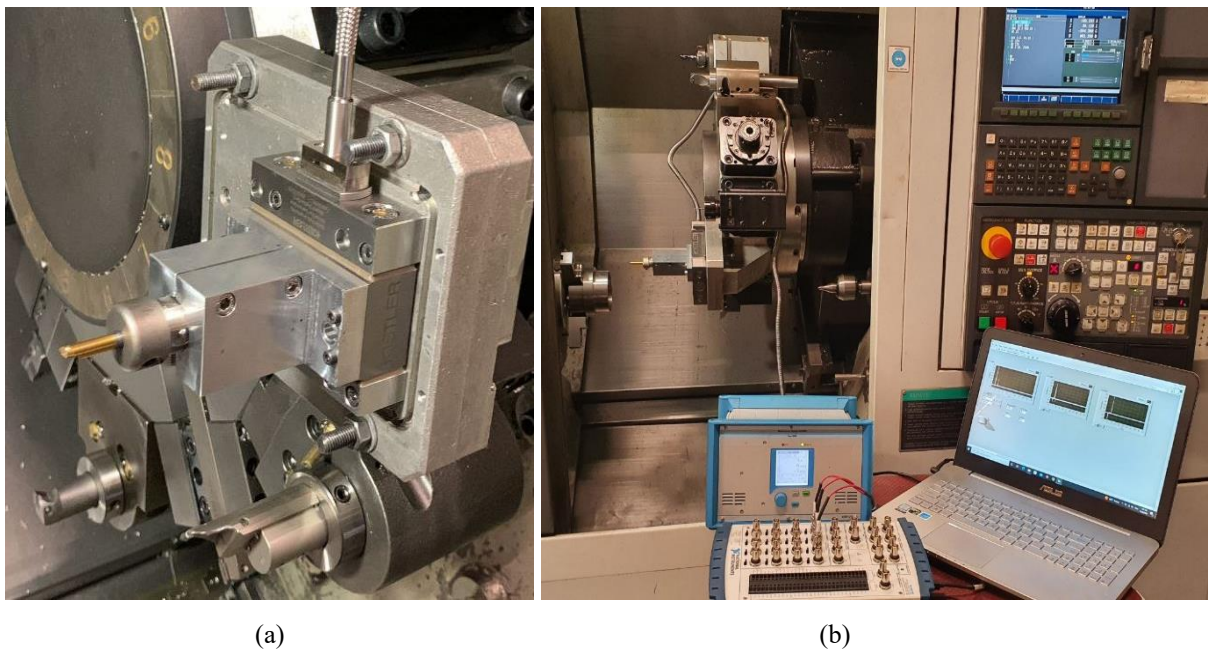


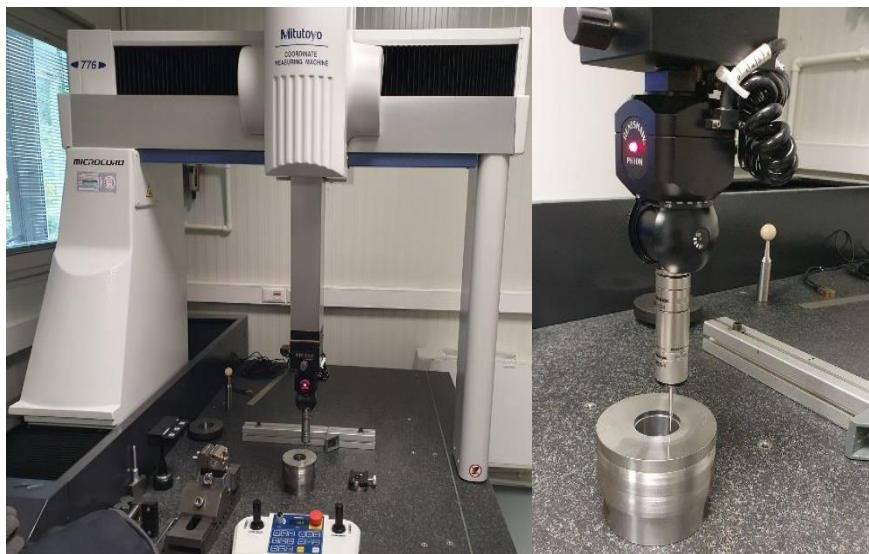
Figure 4.9. a) The fixture used for clamping tool holder on the dynamometer. b) Measuring forces using dynamometer

Cutting tests were conducted in a dry machining condition using sharp tools on the MORI SEIKI NL1500 lathe machine, and the cutting forces were measured using the dynamometer (see Figure 4.9 (b)). After each cutting pass with five different sharp tools (Table 4.6), the workpiece's surface roughness, cylindricity, and circularity were measured using Mahr and CMM machines to evaluate their respective values (see

Figure 4.10). The surface roughness of the hole was measured at four different points, and the average value was recorded. The circularity of the hole was measured using CMM machine at different heights and the cylindricity of the workpiece was obtained by comparing the circularity of these circles (see Figure 4.11).



(a)



(b)

Figure 4.10. a) Measuring the surface roughness of the hole using MarSurf. b) Measuring the circularity and cylindricity of the hole using CMM machine.

Tool T-038 is selected as the control group for comparison with other tools' geometric properties effect on forces and geometric errors. Tool T-042 has a higher hone radius due to a longer honing time, while tools T-043, T-046, and T-047 have higher oblique angle, rake angle, and approach angle, respectively.

Tool T-038 is selected as the control group for comparison with other tools' geometric properties. Tool T-042 has a higher hone radius due to a longer honing time, while tools T-043, T-046, and T-047 have higher oblique angle, rake angle, and approach angle, respectively.

We anticipate higher forces when using tool T-042 due to its larger hone radius, as indicated in Table 4.7.

We expect lower forces when using T-043 and T-046 compared to the forces of tool T-038, but there is a slight increase. Since these force values are small, various factors such as measurement accuracy, noise from other machines during measurement, and variations in hone radius along the cutting edge may contribute to this discrepancy.

As anticipated, since the depth of cut is smaller than the nose radius, the increase in approach angle does not affect the forces when using tool T-047.

Additionally, tool T-038 has a rake angle of 14 degrees, while tool T-046 has a rake angle of 20 degrees. These are high values for the rake angle. Therefore, the increase in forces observed with tool T-046 may be attributed to the fact that a higher rake angle results in a smaller plastic region and a dominant elastic region. In the elastic region, the friction coefficient is higher, potentially leading to increased forces instead of reduction.

The investigation of forces aims to establish a relationship between them, the tool edge's geometric properties, and the surface roughness, cylindricity, and circularity of the final hole after the boring process.

4.2.1 Surface Roughness, Cylindricity, and Circularity

According to the literature on surface roughness, cylindricity, and circularity, the most influential parameters are cutting speed, feed rate, and depth of cut. Each of these parameters has varying effects depending on different cutting conditions, such as the cooling environment, chucking and clamping force, etc.

In our specific case, we conducted the machining process in a dry environment, with a constant feed rate and cutting speed for a particular material. The aim was to illustrate the impact of tool edge geometric properties on surface roughness, cylindricity, and circularity, as shown in Table 4.8.

Table 4.8. Measured geometric errors and surface roughness from experiments.

Tool code	Geometric errors			Surface roughness
	Circularity 1	Circularity 2	Cylindricity	Ra_{avg}
	(μm)	(μm)	(μm)	(μm)
T-038	1	1	1	0.392
T-042	1	1	1	0.807
T-043	1	2	2	0.86375
T-046	1	1	1	0.48375
T-047	1	1	1	0.61575

By examining Table 4.8 it becomes apparent that the geometrical properties do not have an impact on the cylindricity and circularity of the hole. This observation could potentially be attributed to the small values of depth of cut and feed rate employed, which contribute to a more precise boring process.

However, when considering surface roughness, the effect of the tool's geometrical properties becomes evident. Tool T-038, which exhibits the lowest radial force, achieves the lowest surface roughness. Conversely, tool T-043, with a larger oblique angle and higher radial force, yields the highest surface roughness. Additionally, tool T-043 leads to increased circularity and cylindricity errors, indicating that a higher oblique angle is not suitable for improving the tool's performance.

4.2.2 Effect of Tool Wear

The impact of tool wear on the surface roughness, cylindricity, and circularity of the bored hole was experimentally investigated. Two tools (T-038 and T-042) were utilized for 10 passes of cuts at two different depths. The identical cutting conditions were applied, and after 10 passes, the tool wear condition was assessed using a microscope (see Figure 4.12). Furthermore, the surface roughness, cylindricity, and circularity of the bored holes were measured and recorded (refer to Table 4.9).



(a)

(b)

Figure 4.12. a) Wear in the nose of tool T-038 b) Wear in the nose of tool T-042 after 10 passes of cut with 0.12 mm depth of cut

Table 4.9. Measured geometric errors and surface roughness from experiments for worn and sharp tools.

Tool Code	Depth of cut (mm)	Wear condition of tool	Ra_{avg} (μm)	Circularity 1 (μm)	Circularity 2 (μm)	Cylindricity (μm)
T-038	0.12	Sharp	0.392	1	1	1
T-038	0.12	Worn	0.446	3	3	4
T-038	0.25	Sharp	0.403	1	1	1
T-038	0.25	Worn	0.511	1	1	1
T-042	0.12	Sharp	0.807	1	1	1
T-042	0.12	Worn	0.868	5	3	5
T-042	0.25	Sharp	0.803	1	1	1
T-042	0.25	Worn	0.892	2	3	3

Based on the microscope images used to investigate the tool wear condition, it is evident that the most significant wear occurred when tool T-042 was utilized with a depth of cut of 0.12. Consequently, this tool produced the worst circularity and cylindricity results. This can be attributed to the fact that when the depth of cut is smaller than the nose radius, the forces exerted on the tool nose are concentrated, leading to increased damage and wear. As a result, higher levels of geometrical errors are observed.

Additionally, the results indicate that tool T-038, when used with a depth of cut greater than the nose radius, yields better geometrical errors. Although a depth of cut higher than the nose radius improves cylindricity and circularity, it also leads to increased surface roughness. When the depth of cut is high, a larger amount of material is removed from the hole surface, resulting

in reduced geometrical errors. However, higher values of depth of cut generate increased cutting forces, particularly the radial force, which has the most significant impact on surface roughness. Consequently, higher cutting forces result in lower surface quality levels.

4.2.3 Summary of Experimental Results

Experiments were conducted to investigate the influence of tool edge geometrical properties on cutting forces, surface roughness, cylindricity, and circularity during hole enlarging processes using miniature boring tools. Five different tools were selected, with Tool T-038 acting as the control group for comparison. The cutting tests were conducted using sharp tools under specific cutting conditions and 1050 Steel as workpiece.

Experimental results demonstrated that the geometric properties of the cutting edge had a significant impact on surface roughness. The tool identified as T-038, which exerted the least radial force, resulted in the lowest level of surface roughness whereas the tool named T-043, with an increased oblique angle and greater radial force, produced the highest level of surface roughness. Besides, Tool T-043 led to increased circularity and cylindricity errors, which implies that a higher oblique angle did not contribute to the improvement of the tool's performance.

Tool wear was also experimentally investigated, and it was evident that the most significant wear occurred when using Tool T-042 with a depth of cut of 0.12 mm. This resulted in worse circularity and cylindricity values due to concentrated forces on the tool nose leading to increased damage and tool wear.

Furthermore, it was found that Tool T-038 yielded better geometrical errors when used with a depth of cut higher than the nose radius, and the hole's cylindricity and circularity improved. However, this also led to increased surface roughness due to higher forces.

Overall, the study demonstrated the importance of tool edge geometrical properties in influencing cutting forces and surface finish quality after hole enlarging process.

5. Contribution of the Study

This study focuses on investigating the precision of tiny holes generated by miniature boring tools. Unlike previous research on long boring bars, this study explores the effect of the geometrical properties of the tool edge on hole precision and the clamping stiffness of the tool-holder configuration. An analytical force model has been developed to optimize the design of miniature boring tools by minimizing radial forces that can cause tool deviation and poor surface roughness. The study suggests design improvements to the manufacturer based on the investigation's findings. Experiments and simulations are conducted to determine the optimal geometrical parameters of the tool edge, aiming to achieve more precise holes with improved surface roughness, circularity, and cylindricity. These contributions can be summarized as below:

- The effect of the tool's geometrical properties on hole quality was explored for the first time.
- A positive approach angle was considered for the first time in the force and chatter stability model.
- Clamping stiffness for various tool-holder configurations was investigated.
- The design of miniature boring tools was improved using the model.

6. Future Work

Following are the recommended studies for extending the capabilities of the models proposed in this study:

- In the development of the force model, an edge force model could be included to further investigate the impact of hone radius along the nose radius on forces.
- The force model could also be extended to incorporate a tool wear model, which can be subsequently examined through experimental validation.
- Moreover, additional geometrical properties, such as wipers, could be integrated into the tool design. Investigating the effect of wipers on chip geometry and, consequently, on cutting forces could be accomplished through experimental analysis. Furthermore, the impact of wipers on surface roughness can also be studied experimentally.
- To enhance the chatter stability model, the inclusion of mode coupling and process damping effects could be considered.
- A feed rate compensation method during the machining operation could be suggested by analyzing the effect of chuck clamping forces along the entire length of the workpiece.

7. Conclusion

- In this study, an analytical force model is developed based on various configurations of uncut chip geometry. The uncut chip geometry is influenced by the geometrical properties of the cutting tool edge. The model provides accurate predictions of force values through precise chip area calculations. Using this model, the aim was to investigate the effect of tool geometrical properties on cutting forces.
- The main geometrical properties of the cutting edge that affect cutting forces are nose radius, rake angle, oblique angle, and approach angle. The impact of the approach angle becomes evident when the depth of cut exceeds the nose radius. Higher values of positive approach angle lead to lower radial forces.
- The chatter stability model was adapted to predict the stable depth of cut for miniature boring tools with positive approach angles.
- Stiffness measurements and modal analysis of four different tool-holder configurations reveal that the length of the holder and the tool itself influence the stiffness of the tool. However, the most significant factor affecting the rigidity and stiffness of the tool, and consequently the stable depth of cut, is the tolerance of the tool holders used for this type of tools.
- Based on this information, efforts have been made to enhance the design of miniature boring tools by reducing the force values. The objective is to achieve more accurate and precise holes in terms of surface finish quality and geometric errors, such as cylindricity and circularity. By optimizing the geometrical properties of the cutting edge and considering the influence of tool holder tolerance, the aim is to improve the overall performance of the hole enlarging process and achieve higher machining precision.
- The experimental results showed that the geometric properties of the cutting edge significantly influence surface roughness.

- The tool with the least radial force, T-038, resulted in the lowest surface roughness, while T-043, with an increased oblique angle and radial force, produced the highest roughness. T-043 also led to increased circularity and cylindricity errors, suggesting that a higher oblique angle did not improve the tool's performance.
- Tool wear was investigated experimentally, and it was evident that the tool with a depth of cut of 0.12 mm experienced the most significant wear. This depth of cut is smaller than the nose radius, resulting in worse circularity and cylindricity values due to concentrated forces on the tool nose.
- In general, it can be proposed to use a depth of cut higher than the nose radius to take advantage of the positive approach angle in reducing radial forces and achieving lower levels of tool wear. This leads to improved surface finish, circularity, and cylindricity, as well as a longer tool life.

A. Appendix

A. Depth of Cut Higher than Nose Radius

1) Elemental chip thickness for section 1

Section 1 is the region that is formed by the contact points of the new and previous passes at the top of the nose (see Figure 2.8).

For calculating the elemental chip area following elemental values are needed and calculated by Eq. (A.1-A.9):

$$\theta^1 = \frac{\pi}{2} - \cos^{-1}\left(\frac{f}{2r}\right) \quad \text{A.1}$$

$$\theta_j^1 = \frac{\theta^1}{j^1} \quad \text{A.2}$$

$$A^1 = \sum_1^{j^1} A_j^1 \quad \text{A.3}$$

$$A_j^1 \approx A_j^{1'} - A_j^{1''} \quad \text{A.4}$$

$$A_j^{1'} = \left(\frac{1}{2}\theta_j^1 r^2\right) \quad \text{A.5}$$

$$A_j^{1''} = A_{OTT'} = \left(\frac{1}{2}TO_j^1 TO_{j+1}^1 \sin(\theta_j^1)\right) \quad \text{A.6}$$

$$TO_j^1 = \sqrt{f^2 + r^2 - (2fr \cos(\Omega_j^1))} \quad \text{A.7}$$

$$\frac{\overline{OO''}}{\sin\left(\pi - \left(\left(\frac{\pi}{2} - (\theta_j^1(j^1 - 1))\right) + \Omega_j^1\right)\right)} = \frac{\overline{TO''}}{\sin\left(\pi - \left(\frac{\pi}{2} - (\theta_j^1(j^1 - 1))\right)\right)} \quad \text{A.8}$$

$$\Omega_j^1 = \frac{\pi}{2} + (\theta_j^1(j^1 - 1)) - \sin^{-1}\left(\frac{f}{r} \sin\left(\frac{\pi}{2} - (\theta_j^1(j^1 - 1))\right)\right) \quad \text{A.9}$$

2) Elemental chip thickness for section 2 and 3

For the area calculation of sections 2 and 3, the same procedure has to be followed. However, the difference lies in the total angle of the arc. In section 2, the total angle is 90 degrees since it represents a quarter of a circle. In section 3 (refer to Figure 2.8), the total angle is equal to the tool's approach angle.

$$\theta^2 = \frac{\pi}{2} \quad \text{A.10}$$

$$\theta_j^2 = \frac{\theta^2}{j^2} \quad \text{A.11}$$

$$A^2 = \sum_1^{j^2} A_j^2 \quad \text{A.12}$$

$$A_j^2 \approx A_j^{2'} - A_j^{2''} \quad \text{A.13}$$

$$A_j^{2'} = \left(\frac{1}{2}\theta_j^2 r^2\right) \quad \text{A.14}$$

$$A_j^{2''} = A_{OTT'} = \left(\frac{1}{2}TO_j^2 TO_{j+1}^2 \sin(\theta_j^2)\right) \quad \text{A.15}$$

$$TO_j^2 = \sqrt{f^2 + r^2 - (2fr \cos(\Omega_j^2))} \quad \text{A.16}$$

$$\frac{\overline{OO''}}{\sin\left(\pi - (\pi - (\theta_j^2(j^2 - 1))) + \Omega_j^2\right)} = \frac{\overline{TO''}}{\sin(\pi - (\theta_j^2(j^2 - 1)))} \quad \text{A.17}$$

$$\Omega_j^2 = (\theta_j^2(j^2 - 1)) - \sin^{-1}\left(\frac{f}{r} \sin(\pi - (\theta_j^2(j^2 - 1)))\right) \quad \text{A.18}$$

And for section 3 the equations will change as below:

$$\theta^3 = C \quad \text{A.19}$$

$$\theta_j^3 = \frac{\theta^3}{j^3} \quad \text{A.20}$$

$$A^3 = \sum_1^{j^3} A_j^3 \quad \text{A.21}$$

$$A_j^3 \approx A_j^{3'} - A_j^{3''} \quad \text{A.22}$$

$$A_j^{3'} = \left(\frac{1}{2}\theta_j^3 r^2\right) \quad \text{A.23}$$

$$A_j^{3''} = A_{OTT'} = \left(\frac{1}{2}TO_j^3 TO_{j+1}^3 \sin(\theta_j^3)\right) \quad \text{A.24}$$

$$TO_j^3 = \sqrt{f^2 + r^2 - (2fr \cos(\Omega_j^3))} \quad \text{A.25}$$

$$\frac{\overline{OO''}}{\sin\left(\pi - (\pi - (\theta_j^3(j^3 - 1))) + \Omega_j^3\right)} = \frac{\overline{TO''}}{\sin(\pi - (\theta_j^3(j^3 - 1)))} \quad \text{A.26}$$

$$\Omega_j^3 = (\theta_j^3(j^3 - 1)) - \sin^{-1}\left(\frac{f}{r} \sin(\pi - (\theta_j^3(j^3 - 1)))\right) \quad \text{A.27}$$

3) Elemental chip thickness for section 4

This section can be considered as a straight cutting edge (refer to Figure 2.8), so there is no need to divide it into smaller elements.

$$W_n' = r + r \sin C \quad \text{A.28}$$

$$A^4 = A^{4'} + A^{4''} \quad \text{A.29}$$

$$A^{4'} = bf - W_n' f \quad \text{A.30}$$

$$A^{4''} = (TO_{j^2}^2) \sin(C) \quad \text{A.31}$$

B. Depth of Cut smaller than Nose Radius

1) Elemental chip thickness for section 1

The calculation of the chip area in section 1 remains the same as in the previous scenario.

$$\theta^1 = \frac{\pi}{2} - \cos^{-1}\left(\frac{f}{2r}\right) \quad \text{A.32}$$

$$\theta_j^1 = \frac{\theta^1}{j^1} \quad \text{A.33}$$

$$A^1 = \sum_1^{j^1} A_j^1 \quad \text{A.34}$$

$$A_j^1 \approx A_j^{1'} - A_j^{1''} \quad \text{A.35}$$

$$A_j^{1'} = \left(\frac{1}{2} \theta_j^1 r^2\right) \quad \text{A.36}$$

$$A_j^{1''} = A_{OTT'} = \left(\frac{1}{2} TO_j^1 TO_{j+1}^1 \sin(\theta_j^1)\right) \quad \text{A.37}$$

$$TO_j^1 = \sqrt{f^2 + r^2 - (2fr \cos(\Omega_j^1))} \quad \text{A.38}$$

$$\frac{\overline{OO''}}{\sin\left(\pi - \left(\left(\frac{\pi}{2} - (\theta_j^1(j^1 - 1))\right) + \Omega_j^1\right)\right)} = \frac{\overline{TO''}}{\sin\left(\pi - \left(\frac{\pi}{2} - (\theta_j^1(j^1 - 1))\right)\right)} \quad \text{A.39}$$

$$\Omega_j^1 = \frac{\pi}{2} + (\theta_j^1(j^1 - 1)) - \sin^{-1}\left(\frac{f}{r} \times \sin\left(\frac{\pi}{2} - (\theta_j^1(j^1 - 1))\right)\right) \quad \text{A.40}$$

2) Elemental chip thickness for section 2

The logic for calculating the elemental chip thickness remains the same as before, but there is a distinction in the calculation of the area for the first element compared to the other elements.

Area calculation of first element:

$$A_1^2 = A_1^{2'} - A_1^{2''} \quad \text{A.41}$$

$$A_1^{2'} = \left(\frac{1}{2}r^2\theta^{2'}\right) \quad \text{A.42}$$

$$A_1^{2''} = A_{OPK} = \left(\frac{1}{2}r \overline{OK} \sin(\theta^{2'})\right) \quad \text{A.43}$$

$$\theta^{2'} = \pi - O - \theta^{2''} \quad \text{A.44}$$

$$\frac{\overline{KO''}}{\sin(O)} = \frac{\overline{KO}}{\sin(\Omega_1^2)} \quad \text{A.45}$$

$$O = \sin^{-1}\left(\frac{r \sin \Omega_1^2}{\overline{KO}}\right) \quad \text{A.46}$$

$$\overline{KO} = \sqrt{f^2 + r^2 - (2fr \cos(\Omega_1^2))} \quad \text{A.47}$$

$$\Omega_1^2 = \theta^{2''} \quad \text{A.48}$$

$$\theta^{2''} = \sin^{-1}\left(\frac{r - b}{r}\right) \quad \text{A.49}$$

Area calculation of other elements:

$$\theta^2 = \frac{\pi}{2} - (\theta^{2'} + \theta^{2''}) \quad \text{A.50}$$

$$\theta_j^2 = \frac{\theta^2}{(j^2 - 1)} \quad \text{A.51}$$

$$A^2 = \sum_1^{j^2} A_j^2 \quad \text{A.52}$$

$$A_j^2 \approx A_j^{2'} - A_j^{2''} \quad \text{A.53}$$

$$A_j^{2'} = \left(\frac{1}{2}\theta_j^2 r^2\right) \quad \text{A.54}$$

$$A_j^{2''} = A_{OTT'} = \left(\frac{1}{2}TO_j^2TO_{j+1}^2 \sin(\theta_j^2)\right) \quad \text{A.55}$$

$$TO_j^2 = \sqrt{f^2 + r^2 - (2fr \cos(\Omega_j^2))} \quad \text{A.56}$$

$$\frac{\overline{OO''}}{\sin\left(\pi - (\pi - (\theta_j^2(j^2 - 1))) + \Omega_j^2\right)} = \frac{\overline{TO''}}{\sin(\pi - (\theta_j^2(j^2 - 1)))} \quad \text{A.57}$$

$$\Omega_j^2 = (\theta_j^2(j^2 - 1)) - \sin^{-1}\left(\frac{f}{r} \sin(\pi - (\theta_j^2(j^2 - 1)))\right) \quad \text{A.58}$$

Reference

- [1] F. Atabey, I. Lazoglu, and Y. Altintas, “Mechanics of boring processes - Part I,” *Int J Mach Tools Manuf*, vol. 43, no. 5, pp. 463–476, Apr. 2003, doi: 10.1016/S0890-6955(02)00276-6.
- [2] F. Atabey, I. Lazoglu, and Y. Altintas, “Mechanics of boring processes - Part II: Multi-insert boring heads,” *Int J Mach Tools Manuf*, vol. 43, no. 5, pp. 477–484, Apr. 2003, doi: 10.1016/S0890-6955(02)00277-8.
- [3] N. Z. Yussefian, B. Moetakef-Imani, and H. El-Mounayri, “The prediction of cutting force for boring process,” *Int J Mach Tools Manuf*, vol. 48, no. 12–13, pp. 1387–1394, Oct. 2008, doi: 10.1016/J.IJMACHTOOLS.2008.05.003.
- [4] I. Lazoglu, F. Atabey, and Y. Altintas, “Dynamics of boring processes: Part III-time domain modeling,” *Int J Mach Tools Manuf*, vol. 42, no. 14, pp. 1567–1576, Nov. 2002, doi: 10.1016/S0890-6955(02)00067-6.
- [5] E. Budak and E. Ozlu, “Analytical Modeling of Chatter Stability in Turning and Boring Operations: A Multi-Dimensional Approach,” *CIRP Annals*, vol. 56, no. 1, pp. 401–404, Jan. 2007, doi: 10.1016/J.CIRP.2007.05.093.
- [6] B. Moetakef-Imani and N. Z. Yussefian, “Dynamic simulation of boring process,” *Int J Mach Tools Manuf*, vol. 49, no. 14, pp. 1096–1103, Nov. 2009, doi: 10.1016/J.IJMACHTOOLS.2009.07.008.
- [7] D. Östling and M. Magnevall, “Modelling the dynamics of a large damped boring bar in a lathe,” *Procedia CIRP*, vol. 82, pp. 285–289, Jan. 2019, doi: 10.1016/J.PROCIR.2019.04.041.
- [8] C. Mei, “Active regenerative chatter suppression during boring manufacturing process,” *Robot Comput Integr Manuf*, vol. 21, no. 2, pp. 153–158, Apr. 2005, doi: 10.1016/J.RCIM.2004.07.011.
- [9] W. Du, L. Wang, D. Peng, Y. Shao, and C. K. Mechefske, “A new dynamic boring force calculation method using the analytical model of time-varying toolpath and chip fracture,” *J Mater Process Technol*, vol. 306, p. 117642, Aug. 2022, doi: 10.1016/J.JMATPROTEC.2022.117642.

- [10] V. Nguyen, S. Melkote, A. Deshamudre, and M. Khanna, "PVDF sensor based on-line mode coupling chatter detection in the boring process," *Manuf Lett*, vol. 16, pp. 40–43, Apr. 2018, doi: 10.1016/J.MFGLET.2018.04.004.
- [11] W. Du, L. Wang, and Y. Shao, "A semi-analytical dynamics method for spindle radial throw in boring process," *J Manuf Process*, vol. 96, pp. 110–124, Jun. 2023, doi: 10.1016/J.JMAPRO.2023.04.047.
- [12] E. Edhi and T. Hoshi, "Stabilization of high frequency chatter vibration in fine boring by friction damper," *Precis Eng*, vol. 25, no. 3, pp. 224–234, Jul. 2001, doi: 10.1016/S0141-6359(01)00074-5.
- [13] M. H. Miguélez, L. Rubio, J. A. Loya, and J. Fernández-Sáez, "Improvement of chatter stability in boring operations with passive vibration absorbers," *Int J Mech Sci*, vol. 52, no. 10, pp. 1376–1384, Oct. 2010, doi: 10.1016/J.IJMECSCI.2010.07.003.
- [14] E. Abele, M. Haydn, and T. Grosch, "Adaptronic approach for modular long projecting boring tools," *CIRP Annals*, vol. 65, no. 1, pp. 393–396, Jan. 2016, doi: 10.1016/J.CIRP.2016.04.104.
- [15] K. Ramesh, P. Baranitharan, and R. Sakthivel, "Investigation of the stability on boring tool attached with double impact dampers using Taguchi based Grey analysis and cutting tool temperature investigation through FLUKE-Thermal imager," *Measurement*, vol. 131, pp. 143–155, Jan. 2019, doi: 10.1016/J.MEASUREMENT.2018.08.055.
- [16] D. Mei, T. Kong, A. J. Shih, and Z. Chen, "Magnetorheological fluid-controlled boring bar for chatter suppression," *J Mater Process Technol*, vol. 209, no. 4, pp. 1861–1870, Feb. 2009, doi: 10.1016/J.JMATPROTEC.2008.04.037.
- [17] L. Prabhu, S. Satish Kumar, D. Dinakaran, and R. Jawahar, "Improvement of chatter stability in boring operations with semi active magneto-rheological fluid damper," *Mater Today Proc*, vol. 33, pp. 420–427, Jan. 2020, doi: 10.1016/J.MATPR.2020.04.651.
- [18] M. K. A. Saleh, A. Ulasyar, and I. Lazoglu, "Active damping of chatter in the boring process via variable gain sliding mode control of a magnetorheological damper," *CIRP Annals*, vol. 70, no. 1, pp. 337–340, Jan. 2021, doi: 10.1016/J.CIRP.2021.04.039.
- [19] S. Chockalingam, S. Ramabalan, and K. Govindan, "Chatter control and stability analysis in cantilever boring bar using FEA methods," *Mater Today Proc*, vol. 33, pp. 2577–2580, Jan. 2020, doi: 10.1016/J.MATPR.2019.12.166.

- [20] H. Moradi, F. Bakhtiari-Nejad, and M. R. Movahhedy, "Tuneable vibration absorber design to suppress vibrations: An application in boring manufacturing process," *J Sound Vib*, vol. 318, no. 1–2, pp. 93–108, Nov. 2008, doi: 10.1016/J.JSV.2008.04.001.
- [21] L. Houck, T. L. Schmitz, and K. Scott Smith, "A tuned holder for increased boring bar dynamic stiffness," *J Manuf Process*, vol. 13, no. 1, pp. 24–29, Jan. 2011, doi: 10.1016/J.JMAPRO.2010.09.002.
- [22] A. Bansal and M. Law, "A Receptance Coupling Approach to Optimally Tune and Place Absorbers on Boring Bars for Chatter Suppression," *Procedia CIRP*, vol. 77, pp. 167–170, Jan. 2018, doi: 10.1016/J.PROCIR.2018.08.267.
- [23] D. G. Lee, H. Y. Hwang, and J. K. Kim, "Design and manufacture of a carbon fiber epoxy rotating boring bar," *Compos Struct*, vol. 60, no. 1, pp. 115–124, Apr. 2003, doi: 10.1016/S0263-8223(02)00287-8.
- [24] H. Åkesson, T. Smirnova, and L. Håkansson, "Analysis of dynamic properties of boring bars concerning different clamping conditions," *Mech Syst Signal Process*, vol. 23, no. 8, pp. 2629–2647, Nov. 2009, doi: 10.1016/J.YMSSP.2009.05.012.
- [25] J. Niu, J. Hou, Y. Shen, and S. Yang, "Dynamic analysis and vibration control of nonlinear boring bar with fractional-order model of magnetorheological fluid," *Int J Non Linear Mech*, vol. 121, p. 103459, May 2020, doi: 10.1016/J.IJNONLINMEC.2020.103459.
- [26] Y. Altintas, D. Lappin, D. van Zyl, and D. Östling, "Automatically tuned boring bar system," *CIRP Annals*, vol. 70, no. 1, pp. 313–316, Jan. 2021, doi: 10.1016/J.CIRP.2021.04.058.
- [27] A. Aliakbari, G. Moraru, P. Veron, and Y. Groll, "The Effect of a Polymer-Based Tuned Mass Damper on the Vibration Characteristics of an Anti-Vibration Boring Bar," *Procedia CIRP*, vol. 103, pp. 200–206, Jan. 2021, doi: 10.1016/J.PROCIR.2021.10.032.
- [28] W. Takahashi, N. Suzuki, and E. Shamoto, "Development of a novel boring tool with anisotropic dynamic stiffness to avoid chatter vibration in cutting: Part 1: Design of anisotropic structure to attain infinite dynamic stiffness," *Precis Eng*, vol. 68, pp. 57–71, Mar. 2021, doi: 10.1016/J.PRECISIONENG.2020.11.007.
- [29] Z. Iklodi, D. A. W. Barton, and Z. Dombovari, "Bi-stability induced by motion limiting constraints on boring bar tuned mass dampers," *J Sound Vib*, vol. 517, p. 116538, Jan. 2022, doi: 10.1016/J.JSV.2021.116538.

- [30] W. Hintze, M. Hinrichs, O. Rosenthal, U. Schleinkofer, and R. Venturini, "Model based design of tuned mass dampers for boring bars of small diameter," *Procedia CIRP*, vol. 117, pp. 193–198, Jan. 2023, doi: 10.1016/J.PROCIR.2023.03.034.
- [31] W. Thomas, J. Peterka, T. Szabó, M. V. Albuquerque, R. Pederiva, and L. P. Kiss, "Analytical and Experimental Investigation of the Dynamic Stability in Passive Damper Boring Bars," *Procedia CIRP*, vol. 117, pp. 187–192, Jan. 2023, doi: 10.1016/J.PROCIR.2023.03.033.
- [32] Z. Ma, N. A. Henein, W. Bryzik, and J. Glidewell, "Break-In Liner Wear and Piston Ring Assembly Friction in a Spark-Ignited Engine," *Tribology Transactions*, vol. 41(4), pp. 497–504, 1998.
- [33] M. R. Rodrigues and S. F. Porto, "Torque Plate Honing on Block Cylinder Bores," SAE, 1993.
- [34] K. Matsuo et al., "Reduction of Piston System Friction by Applying a Bore Circularity Machining Technique to the Cylinder Block," SAE, 2005.
- [35] J. D. Meadows, "Geometric Dimensioning and Tolerancing Handbook: Applications, Analysis & Measurement," ASME Press, 2005.
- [36] Ni Weihua and Yao Zhenqiang, "Cylindricity modeling and tolerance analysis for cylindrical components," *International journal advanced manufacturing technologies*, vol. 64, pp. 864–874, 2013.
- [37] D. Gao, Y. X. Yao, W. M. Chiu, and F. W. Lam, "Accuracy enhancement of a small overhung boring bar servo system by real-time error compensation," *Precis Eng*, vol. 26, no. 4, pp. 456–459, Oct. 2002, doi: 10.1016/S0141-6359(02)00119-8.
- [38] W. Xiao, Y. Zi, B. Chen, B. Li, and Z. He, "A novel approach to machining condition monitoring of deep hole boring," *Int J Mach Tools Manuf*, vol. 77, pp. 27–33, Feb. 2014, doi: 10.1016/J.IJMACHTOOLS.2013.10.009.
- [39] G. Singh, G. S. Mann, and S. Pradhan, "Improving the Surface roughness and Flank wear of the boring process using particle damped boring bars," *Mater Today Proc*, vol. 5, no. 14, pp. 28186–28194, Jan. 2018, doi: 10.1016/J.MATPR.2018.10.062.
- [40] K. Sørby and D. Østling, "Precision turning with instrumented vibration-damped boring bars," *Procedia CIRP*, vol. 77, pp. 666–669, Jan. 2018, doi: 10.1016/J.PROCIR.2018.08.181.

- [41] M. Lotfi, S. Amini, Z. Aghayar, S. A. Sajjady, and A. A. Farid, "Effect of 3D elliptical ultrasonic assisted boring on surface integrity," *Measurement*, vol. 163, p. 108008, Oct. 2020, doi: 10.1016/J.MEASUREMENT.2020.108008.
- [42] H. P. Ghongade, "Investigation of vibration in boring operation to improve Machining process to get required surface finish," *Mater Today Proc*, vol. 62, pp. 5392–5395, Jan. 2022, doi: 10.1016/J.MATPR.2022.03.561.
- [43] C. H. Kahng, H. W. Lord, and T. L. Davis, "The Effect of Chucking Methods on Roundness Error in the Boring Process," *Journal of Engineering for Industry*, vol. 233, 1976.
- [44] Lei Chen, Juhchin A. Yang, and Albert J. Shih, "Bore Cylindricity in Finish Cylinder Boring," *J Manuf Sci Eng*, vol. 140, 2018.
- [45] I. Korkut and Y. Kucuk, "Experimental Analysis of the Deviation from Circularity of Bored Hole Based on the Taguchi Method," *Journal of Mechanical Engineering*, pp. 340–346, 2010.
- [46] W. THASANA, N. SUGIMURA, K. IWAMURA, and Y. TANIMIZU, "A study on estimation of 3-dimensional surface roughness of boring processes including kinematic motion deviations," *Journal of Advanced Mechanical Design, Systems, and Manufacturing*, vol. 4, 2014.
- [47] C. Chandrasekhara Sastry, K. Gokulakrishnan, P. Hariharan, M. Pradeep Kumar, and S. Rajendra Boopathy, "Investigation of boring on gunmetal in dry, wet and cryogenic conditions," *Journal of the Brazilian Society of Mechanical Sciences and Engineering*, pp. 16–42, 2020.
- [48] C. Chandrasekhara Sastry, P. Hariharan, M. Pradeep Kumar, and M. A. Muthu Manickam, "Experimental investigation on boring of HSLA ASTM A36 steel under dry, wet, and cryogenic environments," *Materials and Manufacturing Processes*, no. 1042–6914, 2019.
- [49] Y. Altintas, *Manufacturing Automation*. 2012.
- [50] E. Budak and E. Ozlu, "Development of a thermomechanical cutting process model for machining process simulations," *CIRP Annals*, vol. 57, no. 1, pp. 97–100, Jan. 2008, doi: 10.1016/J.CIRP.2008.03.008.
- [51] E. Budak and E. Ozlu, "Analytical Modeling of Chatter Stability in Turning and Boring Operations: A Multi-Dimensional Approach," *CIRP Annals*, vol. 56, no. 1, pp. 401–404, Jan. 2007, doi: 10.1016/J.CIRP.2007.05.093.

[52] “MAL Inc. – Virtual machining & optimization solutions.” <https://www.malinc.com/> (accessed Jul. 24, 2023).